THERMODYNAMIC PROPERTIES AND PHASE RELATIONS IN MANTLE MINERALS INVESTIGATED BY FIRST PRINICIPLES QUASIHARMONIC THEORY

Renata M. Wentzcovitch
Department of Chemical Engineering and Materials Sciences and Minnesota Supercomputer Institute, University of Minnesota, Minneapolis, MN 55455

Yonggang G. Yu
Department of Geosciences Virginia Polytechnic Institute and State University, Blacksburg, VA 24060

Zhongqing Wu
[3]Department of Physics, University of South California, Los Angeles, CA 90007

INTRODUCTION

This research has been motivated by geophysics and materials physics. The objective has been to advance materials theory and computations for high pressure and high temperature applications to the point that it can make a difference in our understanding of the Earth. Understanding of the mineralogy, composition, and thermal structure of the Earth evolves by close interaction of three fields: seismology, geodynamics, and mineral physics. Earth's structure is imaged by seismology, which obtains body wave velocities and density throughout the Earth's interior (Fig. 1). Interpretation of this data relies on knowledge of aggregate properties of Earth forming materials either measured in laboratory or calculated, in many cases by both. However, the conditions of the Earth's interior, especially at the core, may be challenging for important experiments, and materials computations have emerged to contribute decisively to this field. Earth's evolution is simulated by geodynamics, but these simulations need as input information about rheological and thermodynamic properties of minerals, including phase transformation properties such as Clapeyron slopes. Our research has concentrated on the phases of the Earth's mantle, particularly the deep mantle whose conditions are more challenging for experiments. The mantle accounts for ~83% of the Earth's volume. In this article we will review the essential first-principles approach used to investigate solids at high temperatures and pressures, summarize their performance for mantle minerals (Fig. 2), and point to critical results that have stirred us in the current research path. The success is remarkable, but some limitations point the way to future developments in this field.

The methods used in this research are parameter free, based on density functional theory (DFT) (Hohenberg and Kohn 1964, Kohn and Sham 1965) and the quasiharmonic approximation (Born and Huang 1956). The established framework used to describe the

total energy of a system of electrons and ions, DFT, performs very well for most silicates and oxides of the mantle. The theoretical foundation of DFT is reviewed by John Perdew in this issue. Several approximations to the exchange-correlation functional are reviewed and tested in molecular clusters by Donald Truhlar in this issue also. For minerals containing iron it is necessary in general, to go beyond DFT. Matteo Cococcioni reviews in this issue the first-principles DFT plus Hubbard U (DFT+U) method (Anisimov et al. 1991). The DFT+U functional is an *ansatz*, but U is not a free parameter. It is determined consistently using linear response theory (Cococcioni and de Gironcoli 2005). Applications of this method are discussed also in the chapter on spin crossovers in iron-bearing minerals in this book.

A word must be said about pseudopotentials. They are numerically engineered entities that replace the potential generated by the atomic nuclei and core electrons. They can be obtained by several methods. One might contend that they are not parameter free. They use cut off radii in the numerical manipulation of the valence electron wavefunctions in the process of generating the pseudopotential. However, these parameters are not really free. They have optimum values that maximize the pseudopotential transferability to environments other than the atom while simultaneously maximizing their "smoothness". The latter is important to speed up plane-wave calculations which use their Fourier transforms. These two criteria create a tug-of-war in the choice of cut-off radii: smoothness improves by increasing cut-off-radii while transferability improves by decreasing them. The optimum set of radii depends on the degree one is willing to compromise on smoothness or transferability. For this reason several methods to generate pseudopotentials have been proposed (Hamann et al. 1979, Vanderbilt 1990, Troullier and Martins 1991). They have evolved with the aim of decreasing the conflict imposed by these two requirements. Experience matters in generating pseudopotentials. Results are sensitive to their quality. However, a good pseudopotential should represent well an atom core in any environment, in any material. Broadly speaking, this is the ultimate guiding principle for pseudopotential generation.

In this article we review the systematic performance of two popular exchange-correlations functionals, the local density approximation (LDA) (Ceperley and Alder 1980, Perdew and Zunger 1981) and the generalized gradient approximation of Perdew, Burke, and Ernzerhof (PBE-GGA or GGA for short) (Perdew et al. 1996) combined with quasiharmonic theory and first principles phonons obtained using density functional perturbation theory (DFPT) (Baroni et al. 2001). Density functional theory as applied to phonons is reviewed by Stefano Baroni *et al*. in this book. The performance of these functionals is examined on mantle silicates and oxides. Probably the most important message here is the critical role played by zero point motion on the structural properties (lattice parameters, compressibilities, etc). Hence, inferences regarding the performance of various exchange correlation functionals should take this effect into account.

Here we need to discuss the quasiharmonic approximation (QHA) and its performance in some details. Its application to minerals at mantle conditions has been viewed with some skepticism in the past (or even today). Obviously, its application must be limited to a certain temperature range before anharmonic effects become non-

negligible. Therefore, the question becomes: how small are anharmonic effects for minerals at relevant conditions of the mantle? We have been guided by the relationship between the measured melting temperature, T_M, of mantle phases and the expected mantle temperatures (see Fig. 3). More will be said about this later, but the latter is ~ 2/3 of the former in most of the mantle, except in the ~300 km above the core-mantle boundary, where the temperature rises to ~4,000 K. Therefore, the QHA is expected to be a good approximation for most of the mantle, but maybe questionable near the core mantle boundary. Comparisons of QHA results with experiments are very helpful in addressing this question. Ideally one would want to compare QHA predictions with results of molecular dynamics (MD) simulations. However, MD results should be converged with respect to the number of atoms, and have small statistical errors to allow for such comparisons. QHA results correspond to dynamics on more than 10^4 atoms.

We have also investigated the magnitude of anharmonic effects at mantle conditions, where experimental results are not usually available. We have developed an approximate functional form for the anharmonic free energy parameterized to *some* experimental data on a material and used it to reproduce *all* available experimental thermodynamic data on the same material (Wu and Wentzcovitch 2009). This anharmonic free energy is then extended to mantle conditions to investigate anharmonic effects on thermodynamic properties and phase boundaries. This was a pedagogical exercise that revealed multiple manifestations of anharmonicity. This approximation assumes that all phonons are stable in the pressure and temperature range investigated. Therefore, it should not be applicable to unstable structures stabilized by anharmonic fluctuations, such as $CaSiO_3$-perovskite (Stixrude et al. 2007).

A disclaimer is in order. We will not discuss extensively first-principles results obtained by others on the phases analyzed here. Conclusions regarding the performance of first-principles methods can be drawn more safely by comparing results generated systematically, using the same pseudopotentials, and with a homogeneous quality control standard.

THE QUASIHARMONIC APPROXIMATION (QHA)

The QHA is a simple yet effective approximation to thermodynamics properties of crystals. Its effectiveness has become more evident with the advent of first-principles phonons (Gianozzi et al 1991). This approximation treats phonons as if they did not interact, as a phonon "gas". The system becomes equivalent to a collection of independent harmonic oscillators. If the phonon frequencies are known, the energy levels of the system are well defined, and the partition function and Helmholtz free energy can be calculated. From the latter, all thermodynamic properties can be defined. The partition function, Z, of one oscillator with frequency ω is the summation of the Boltzmann factors of all of its energy levels:

$$Z_i = \sum_{j=0}^{\infty} e^{-\frac{\varepsilon_j(\omega_i)}{k_B T}}, \qquad (1)$$

where $\varepsilon_j(\omega_i) = (j + \frac{1}{2})\hbar\omega_i$ (i.e. $\frac{1}{2}\hbar\omega_i, \frac{3}{2}\hbar\omega_i, \frac{5}{2}\hbar\omega_i, ...$) are the energy levels of the oscillator. This summation can be contracted as

$$Z_i = \frac{e^{-\frac{\hbar\omega_i}{2k_BT}}}{1 - e^{-\frac{\hbar\omega_i}{k_BT}}} \tag{2}$$

and the Helmholtz free energy of this oscillator, $F_i^{th} = -k_BT \ln Z_i$, becomes

$$F_i = \frac{1}{2}\hbar\omega_i + k_BT \ln\left(1 - e^{-\frac{\hbar\omega_i}{k_BT}}\right) \tag{3}$$

For a lattice with vibrational modes with frequencies ω_i, the total free energy is

$$F = E + \sum_i F_i^{th} = U + \sum_i \frac{1}{2}\hbar\omega_i + k_BT \sum_i \ln\left(1 - e^{-\frac{\hbar\omega_i}{k_BT}}\right) \tag{4}$$

where U is the internal energy, in our case the static DFT energy. As the solid compresses and deforms elastically, E, ω_i's, and F change. With e_{ij}'s as Lagrangian strains defining elastic deformation of a pre-compressed state, the free energy $F(V,T,e_{ij})$ can be used to derive all thermodynamics and thermoelastic properties of the solid. Thermoelasticity is addressed in the article by Wentzcovitch et al (2010) in this book, so, here e_{ij}'s are zero. Pressure and entropy are:

$$S = -\left(\frac{\partial F}{\partial T}\right)_V, \tag{5-a}$$

$$P = -\left(\frac{\partial F}{\partial V}\right)_T, \tag{5-b}$$

and the thermodynamic potentials can be evaluate in straightforward manner after $V \leftrightarrow P$ variable interchange, if necessary.

$$E = F + TS, \tag{6-a}$$
$$H = E + PV, \text{ and} \tag{6-b}$$
$$G = F + PV. \tag{6-c}$$

This is the standard quasiharmonic thermodynamic formalism which we refer to as "statically constrained" QHA (Carrier et al 2007). In this approach, by construction, phonon frequencies and crystal structures are uniquely related to the volume, irrespective of temperature. This relationship is established by static calculations that optimize crystal structures for a set of chosen pressures (Wentzcovitch et al 1993). Phonon frequencies are then calculated for these structures, and neither of them changes with temperature after this point. Only pressure changes with temperature at these volumes. This fact has significant implications, particularly for thermoelasticity (Carrier et al 2007, *ibid* 2008), but this discussion will be deferred to the next paper on thermoelasticity of minerals. As is, the statically constrained QHA is a very effective approach to study the thermodynamics of solids at low temperatures but not at high temperatures where phonon-phonon interactions, or anharmonic effects, are important. At high T, such as

near-melting temperatures, the dynamics of ions is more appropriately treated by classical MD (Oganov et al 2001). The Debye temperature, Θ_D, is the conventional upper limit of applicability of the QHA, but we have suggested a more direct criterion based on an *a posteriori* inspection of the thermal expansivity (Wentzcovitch et al 2004, Carrier et al 2007).

In this paper we also review phase relations in the most important mantle phases. Direct comparison of the Gibbs free energy of phases establishes their thermodynamic phase boundary. Phase transitions in mantle minerals produce important mantle velocity and density discontinuities. Uncertainties in the experimentally determined phase boundaries are still significant and calculations have a role to play if they can be predictive. Here we summarize the performance of the most popular exchange-correlation functionals, LDA and PBE-GGA (GGA hereafter) in the prediction of phase boundaries between mantle silicates.

THERMODYNAMIC PROPERTIES OF MANTLE PHASES

In first approximation, Earth is spherically homogeneous and has a layered structure. Crust, mantle, and core are the three layers with distinct chemical compositions (Fig. 1). Boundary discontinuities within these layers indicate sharp phase changes induced by pressure and temperature. Lateral velocity variations are more subtle and tell much about the Earth's dynamics. They are primarily related with lateral variations of temperature, subtle chemical composition, and mineralogy. Together with knowledge of the thermodynamic properties of minerals, lateral velocity variations provide essential information for geodynamic modeling. The latter aims to describe the Earth's dynamic evolution.

The main theme of our work is the silicate mantle with its own internal layers and the minerals that comprise this region. At mantle boundary layers, phase transitions between predominant minerals are taking place. These boundaries are ~ 10 km wide, the width being related with phase loops intrinsic to multi-phase multi-component aggregates of the mantle in thermodynamic equilibrium (see chapter by Lars Stixrude in this book). They also have topography related with lateral variations of temperature, chemical composition or mineral phases (see Fig. 2). Knowledge of these mineral phase boundaries helps to understand conditions and processes taking place at these mantle boundary layers. In contrast with the Earth's crust, which is composed of a tremendous variety of mineral phases, the Earth's mantle appears to be relatively simple and consists of few mineral phases (see Figs 1 and 2).

Despite the small number of phases, they are solid solutions co-existing in thermodynamic equilibrium. Description of such complex systems poses challenges to first-principles calculations and must be addressed in installments. Semi-empirical approaches to thermodynamic equilibrium, such as that reviewed by Stixrude in this book, are currently the most practical. Mantle solid solutions are primarily magnesium-iron silicates and oxides, some containing aluminum or calcium also. In addition, the iron bearing phases of the lower mantle undergo spin crossovers. Properties of some of these

systems are reviewed by Hsu *et al*. in this book. Here we discuss primarily the magnesium end member phases. Our calculations are consistent and systematic using the same set of pseudopotentials with the same convergence criterion (see appendix for computational details including pseudopotential information). These systematic results allow one to assess the performance of the LDA and GGA for these systems and to infer trends reliably.

MgO

MgO in the rocksalt structure is the primary end-member of ferropericlase, $(Mg_{(1-x)}Fe_x)O$ (x~0.18), the second most abundant mineral phase in the Earth's lower mantle after Al-$(Mg,Fe)SiO_3$ (*Pbnm*) perovskite. As a simple monoxide, it was a good test-case for the first-application of QHA along with the LDA and PBE-GGA. The calculated phonon dispersions of MgO (Karki et al. 1999, 2000a) using DFPT (Baroni et al. 2001) are in excellent agreement with neutron scattering experiments by Sangster et al. (1970) (see Fig. 4). This demonstrates the success of LDA and the linear response theory applied to ionic crystals. The calculated phonon dispersion and density of states are then used along with Eq. 4 to compute the Helmholtz free energy from which volume vs. pressure relations at various temperatures are obtained. The result is shown in Fig. 5. The dashed line corresponds to static free energy results (0 K DFT results without zero point motion energy). The black solid line corresponds to results at 300 K. The difference between the two curves is caused primarily by zero point motion (2nd term on the r.h.s. of Eq. 4) which is positive, and to a lesser extent by the thermal excitation energy (3rd term on the r.h.s. of Eq. 4) which is negative. The free energy shift from static values to 300 K values is more acute at smaller volumes owing to increased values of ω's at high pressures, as shown in Fig. 4. The dependence of individual phonon frequency on volume is quantified by the mode Grüneisen parameter (γ_i), defined as $\gamma_i = \frac{d \ln \omega_i}{d \ln V}$ with i labeling modes. With increasing temperature, free energy decreases quickly owing to the 3rd term in Eq. 4. Starting from *F(V,T)*, we calculate other thermodynamic potentials and all thermodynamic properties as functions of P and T. These include volume, V, thermal expansivity, α, isothermal bulk modulus and its derivatives, K_T and K_T', isobaric heat capacity, C_p, and thermal Grüneisen parameter, γ_{th} (see Table 1).

The LDA results shown here are in excellent agreement with experimental measurements at ambient conditions. The LDA values for V, K_T and K_T', α, C_p, and γ_{th} are all within at most 0.5% from experimental values, while the GGA results deviate more. Specifically, the LDA equilibrium volume at 300 K is only slightly 0.2 % larger than experiments, but GGA overestimates volume by 2.0%. The LDA bulk modulus lies within experimental uncertainties, but the GGA underestimates it by 2%. The predicted LDA thermal expansivity agrees with experiments while the GGA overestimates it by 3 %. Similar situation occurs for C_p and γ_{th}. In general, LDA results for thermodynamic, structural, and elastic properties of magnesium silicates and oxides within the QHA are in much better agreement with experiments than the GGA. The opposite is observed for static calculations. This demonstrates the importance of considering vibrational effects

before comparing the performance of various exchange-correlation functionals for structural properties. Complete analysis of these thermodynamic properties at high pressures and temperatures can be found in Karki et al. (2000a).

$MgSiO_3$-perovskite

$MgSiO_3$-perovskite (see Fig. 6a) is the primary end member of the most abundant mineral phase of the lower mantle, $(Mg_{(1-x)},Fe_x)SiO_3$ (x~0.12). Accurate knowledge of high *P-T* thermodynamic properties of this phase is a central ingredient for understanding and modeling the lower mantle. Full LDA phonon dispersions of $MgSiO_3$ perovskite are shown in Fig. 7 (Karki et al. 2000b). Predicted Raman and infrared frequencies at 0 GPa compare very well with experimental values (Karki et al. 2000b, Wentzcovitch et al. 2004). Fig. 8 shows the LDA thermal expansivity of perovskite predicted by the QHA and compared with some direct experimental measurements (symbols), some indirect values derived from experimental information (thick inclined dashed lines), and MD calculations using the GGA (horizontal thin dashed lines) (see caption). Fig. 8 conveys essential information about the QHA: at low temperatures, its predictions are in excellent agreement with experimental measurements. At high temperatures its prediction departs quickly from the experimentally observed linear temperature dependence. This deviation is suppressed with increasing pressure, and the behavior becomes more linear and agrees better with experimental data up to higher temperatures. As will be seen in the last section, thermal expansivity is most sensitive to anharmonicity. This deviation is caused by the inadequacy of the QHA at high temperatures where phonons interact more strongly. This behavior of the QHA based thermal expansivity naturally suggests a criterion to establish its upper temperature limit of validity. This is determined by the position of inflection point in $\alpha(T,P=cte)$, i.e., by $\left.\frac{\partial^2\alpha}{\partial T^2}\right|_P = 0$. This limit is shown as a function of pressure by the black dots connected by a broken line in Fig. 8.

This criterion places lower mantle temperatures well within the regime of validity of the QHA (see Fig. 9), except perhaps at the entrance of the lower mantle, around 23 GPa and lower pressures, including perhaps ambient conditions. Indeed, $MgSiO_3$ perovskite is a metastable phase below 23 GPa. For other phases such as MgO and a very different material, metallic aluminum, investigation of this criterion shows that it is a very sensible one. The inflection point versus pressure is usually located well below the melting line (see Fig. 10). Therefore, the position of this inflexion point can be used as the lowest bound estimate for melting temperatures at tens of Mbar when measurements are virtually impossible (Umemoto et al. 2006).

The predicted thermodynamic propertied of perovskite (Karki et al 2000b, Tsuchiya et al. 2005) are in quite good agreement with experimental values, some of which still have large uncertainties. The predicted LDA equilibrium volume at ambient conditions is ~1% larger than the experimental volume. The bulk modulus is expected to be a little smaller, falling in the lower end of the experimental range of values. The thermal expansivity and thermal Grüneisen parameter fall well in the experimental range. The specific heat is ~3% larger. Among the systems investigated this is the worst

performance of LDA/QHA found (see Table 1), and we suspect of the non-obvious inadequacy of the QHA at 0 GPa. The GGA predicts considerably worse results. This point is discussed further in this issue in a paper by Wentzcovitch et al (2010) on thermoelastic properties of minerals. Complete discussion of the thermodynamic properties of perovskite at high pressures and temperatures can be found in Karki et al. (2000b), Wentzcovitch et al 2004, and Tsuchiya et al. (2005).

$MgSiO_3$ post-perovskite

$MgSiO_3$ post-perovskite has the $CaIrO_3$ type structure (*Cmcm*) shown in Fig. 6b, is the latest found mineral of the lower mantle (Murakami et al. 2004, Tsuchiya et al. 2004, Oganov and Ono 2004). It is presumably the most abundant mineral in the D" region of the mantle, i.e., ~250 km above the core mantle boundary (CMB). Pressures and temperatures in this region are expected to be above 125 GPa and 2500 K. Its discovery rejuvenated geophysical interest on this region and on the ultra-low velocity zone, the 5-10 km layer adjacent to the CMB. $MgSiO_3$ post-perovskite appears to be very anisotropic at first glance since it has a layered structure. The LDA calculated equation of state parameters are in excellent agreement with those obtained from in situ volume measurement by Komabayashi et al. (2008), while the GGA equation of state is considerably worse. This mineral is nearly unstable at ambient conditions (Tsuchiya et al. 2005). The seeming large discrepancy between the measurement and the LDA prediction of its thermal expansivity, ~30% is misleading, because experimentally post-perovskite is unattainable at ambient conditions and its ambient thermal expansivity was assumed to be the same as that of the perovskite ($1.67\ K^{-1}$) by Komabayashi et al. (2008) in their experimental fittings. At lower mantle conditions, the QHA is expected to predict very well its thermodynamic properties (see Fig. 9). At shallow mantle conditions, where post-perovskite is (almost) unstable, and at the core-mantle boundary, where the temperature can reach 4,000 K, QHA's performance may be questionable. Detailed comparison between the thermodynamic properties of $MgSiO_3$ perovskite and post-perovskite at high pressures and temperatures can be found in Tsuchiya et al. (2005). Briefly, all the thermodynamic properties of these two phases become more similar with increasing pressure. At ~125 GPa, the pressure at the D" discontinuity, and beyond they are almost indistinguishable (Tsuchiya et al. 2005).

SiO_2 stishovite

Stishovite is one of the high pressure phases of silica (SiO_2). It has the rutile structure (Fig. 11), the natural form of TiO_2 with $P4_2/mnm$ symmetry. A salient feature in stishovite is that the coordination number of silicon by oxygen is 6 rather than 4, the latter is the case for quartz and coesite, low pressure form of silica. Other silicates that contain SiO_6 octahedra include majorite (partially tetrahedral and octahedral), ilmenite, perovskite, and post-perovskite. Overall good agreement is found between the predicted LDA equilibrium volume and thermodynamic properties and experimental values (Akaogi et al. 1995, Andrault et al. 2003). DFT calculations on stishovite can also be found in Oganov et al. (2005), Umemoto et al. (2006).

Mg_2SiO_4 forsterite (α-phase)

Forsterite (the α-phase Mg_2SiO_4), is the end member of the dominant phase in the upper mantle, olivine ($(Mg_{(1-x)}Fe_x)_2SiO_4$, with x~0.012). The orthorhombic crystal structure (*Pbnm*) is shown in Fig 12. Oxygens form a distorted hexagonal close packed (HCP) sublattice; SiO_4 tetrahedra form isolated islands; divalent cations, such as magnesium, occupy octahedral sites. Owing to its abundance, Mg_2SiO_4 forsterite has been thoroughly studied experimentally, e.g., its vibrational spectroscopy and thermal elasticity have been measured (Chopelas 1990), and its equation of state parameters determined from experiments (e.g. Guyot et al. 1996, Downs et al. 1996, Gillet et al. 1991, Bouhifd et al. 1996) and calculated by various methods (Price et al. 1987, Li et al. 2006). The thermodynamic properties of forsterite calculated by LDA and GGA are compared with experiments and shown in Table 1. The ambient conditions LDA results are in excellent agreement with experiments despite the detection of anharmonic effects in some zone center modes (e.g., Gillet et al. 1991). GGA overestimates the volume by 4%, underestimates the thermal expansivity by ~15%, and overestimates the heat capacity by ~4.5% compared with experiments and LDA results. Due to the larger volume predicted by the GGA, the GGA bulk modulus is ~10% smaller than the experimental counterpart. Extensive analysis of the high pressure and high temperature thermodynamic properties of forsterite can be found in Li et al. (2007).

Mg_2SiO_4 wadsleyite (β-phase)

Wadsleyite, the β-phase Mg_2SiO_4 has a modified spinel structure. It was discovered by Ringwood and Major (1966) during the process of compressing high-magnesium olivine. It has a stability field in-between that of forsterite and ringwoodite, the true spinel phase. It is a major phase in Earth transition zone (from 410km to 660 km depth). The wadsleyite crystal structure has body centered orthorhombic symmetry with space group *Imma*. This structure contains pairs of corner sharing SiO_4 tetrahedra forming a Si_2O_7 unit, while leaving one oxygen non-bonded by silicon in the structure (see Fig. 12). This non-silicate oxygen appears to be a good site for hydrogen attachment. For this reason wadsleyite has received great attention as a promising water storage candidate in Earth transition zone (e.g. Smith et al. 2005). As seen in Table 1, the agreement between LDA predictions (Wu and Wentzcovitch, 2007) and measurements (Hazen et al. 1990, 2000; Horiuchi and Sawamoto 2000; Suzuki et al. 1980; Ashida et al. 1987) at ambient conditions for equilibrium volume, bulk modulus and other thermodynamic properties is outstanding. High pressure and high temperature thermodynamic properties of wadsleyite can be found in Wu and Wentzcovitch (2007).

Mg_2SiO_4 ringwoodite (γ-phase)

Mg_2SiO_4 ringwoodite has the spinel structure with Fd-3m symmetry, which consists of isolated SiO_4 tetrahedra (see Fig. 12). The oxygen sublattice forms an FCC-like structure with magnesium ions occupying interstitial sites between SiO_4 groups. LDA predictions for all thermodynamic properties at ambient condition are in outstanding agreement with experiments (see Table 1). High pressure and high

temperature thermodynamic properties of ringwoodite have been analyzed in detailed by Yu and Wentzcovitch (2008). High temperature equations of state and thermodynamics properties are in good agreement with experimental measurements of Meng et al. (1994), Chopelas et al. (1994), Li (2003), Jackson et al. (2000), Weidner et al. (1984), Katsura et al. (2004b), Suzuki et al. (1979), Chopelas (2000). Results are also consistent with the thermodynamics properties deduced from limited Raman and IR spectroscopy by Chopelas et al. (1994). The thermoelastic properties of this phase have also been investigated using MD (Li et al 2006b).

Low and high pressure $MgSiO_3$ clinoenstatite

$MgSiO_3$ low-pressure clinoenstatite ($P2_1/c$, denoted by LP-En) and high-pressure clinoenstatite ($C2/c$, denoted by HP-En) are also important constitutes of Earth upper mantle (CPx in Fig. 2). LP-En exists at ambient conditions while HP-En had eluded unambiguous experimental detection until 1990s because it is unquenchable and converts into LP-En under decompression. Both LP-En and HP-En exist in monoclinic structures with obtuse monoclinic angles (see Fig. 13). In LP-En there are two symmetrically distinct SiO_4 tetrahedral chains (S, and O chain) with two different kinked chain angles, while in HP-En only one exists (O chain, see Fig. 13). A lattice dynamics study of LP-En (Yu and Wentzcovitch, 2009) showed that its lowest *Ag* mode softens slightly under pressure. It was also shown that the *Ag* displacement mode can convert the S-chain in LP-En into the O-chain in HP-En. For these two complex and subtle silicate chain structures, we still observe excellent agreement between the predicted LDA thermodynamic properties and experimental measurements (see Table 1) by Angel and Hugh-Jones (1994), Shinmei et al. (1999). Thanks to DFT we also identified one viable transition path related to the *Ag* mode connecting the two enstatite chain structures (Yu and Wentzcovitch 2008). High temperature and high pressure theremodynamic properties of this mineral can be found are extensively discussed in Yu et al. (2009).

$MgSiO_3$ ilmenite

$MgSiO_3$ ilmenite has a trigonal structure with space group *R-3*. This structure derives from corundum structure (Al_2O_3) except that the octahedral layers contain alternating cations (see Fig. 14). Oxygens form a distorted HCP sublattice, while both magnesium and silicon are in 6-fold octahedral sites (Fig. 14). Ilmenite is a high pressure phase for $MgSiO_3$ but only at relatively low temperatures compared with the mantle geotherm. But it should exist in cold slabs. $MgSiO_3$ ilmenite is stable approximately between 21 to 25 GPa at 1373 K (Ito and Yamada, 1981). With increasing temperature and pressure, the ilmenite phase transforms to the *Pbnm* perovskite or to the garnet phase depending on temperature, pressure, and possibly solid solution composition (Ito and Yamada 1981, Liu 1977). Our LDA results are in reasonably good agreement with experiments. Note that depending on different pressure scales, the experimentally determined K' can vary from 7.5 to 5.6 (Reynard et al. 1996). Our calculations are performed in a larger pressure range (e.g. to 50 GPa) than the experiment (to 28 GPa) by Reynard et al. (1996) and the resulting equation of state parameters are expected to be more reliable. Detailed analysis of the high temperature and high pressure

thermodynamic properties of this mineral can be found in Karki and Wentzcovitch (2002). The thermoelastic properties of this phase have also been investigated using MD (Li et al 2009).

$MgSiO_3$ majorite

The magnesium end-member garnet, $Mg_3(MgSi)Si_3O_{12}$, is called majorite. At ~18 GPa and room temperature the stable phase is accepted to be a body-centered tetragonal (bct) phase ($I4_1/a$) with c/a ~ 0.98 (Angel et al. 1989; Heinemann et al. 1997). The single crystal experiment by Angel et al. (1989) revealed twin structures with slightly disordered (~20%) magnesium and silicon octahedral sites. At high temperatures (e.g. 2000^o C), it has been shown that this tetragonal phase transforms to cubic (*Ia-3d*) with magnesium and silicon completely disordered within the octahedral sites. Also, an intermediate structure with space group $I4_1/acd$ has been proposed in the literature (Nakatsuka 1999; Hofmeister et al. 2004). Fig. 14 shows the tetragonal majorite structure in which one quarter of the silicon ions are in (dark) octahedral sites and the other three quarters are in tetrahedral sites. Magnesium ions are also grouped into two types: one type at center of (light) octahedra and the other type at the center of dodecaheddra (spheres). The LDA equation-of-state parameters are in excellent agreement with the single crystal X-ray study of Angel et al. (1989). Thermodynamic properties at high pressures and temperatures will be reported in the near future (Yu et al., 2010). The thermoelastic properties of this phase have also been investigated using MD (Li et al 2007).

CaO

CaO is not a mantle mineral *per se* but it is a component in mantle minerals. Despite the similarity between rocksalt CaO and MgO, CaO appears to be an anharmonic crystal (Karki and Wentzcovitch 2003). It transforms into a CsCl-type structure at ~50-56 GPa (Jeanloz et al. 1979). Phonon calculations indicate that both phases have stable phonons in the 50-60 GPa range (Karki and Wentzcovitch 2003) but phonons soften in NaCl- and become unstable in CsCl-type CaO in the vicinity of the transformation. Therefore the applicability of the QHA in the vicinity of the transition pressure is questionable. In overall, experimental equation of state parameters and thermodynamic properties at 300 K (Oda et al 1992) are not well reproduced by QHA calculations. V_0 is ~5% smaller, K_T ~10% larger, α ~15% larger, γ_{th} ~25% larger, C_P ~ 35% larger. The more polarizable nature of calcium may induce anharmonicity in the vibrations.

$CaSiO_3$ perovskite

$CaSiO_3$ perovskite is an important lower mantle phase but it is unquenchable to ambient pressure (Wang and Weidner 1994). It is a strongly anharmonic crystal (Stixrude et al 1996). At lower mantle pressures and temperatures it has cubic symmetry (*Pm-3m*) but the symmetry is reduced to tetragonal (*I4/mcm*) at high pressures and low temperatures (Shim et al. 2002, Caracas et al 2005, Caracas and Wentzcovitch 2006, Stixrude et al. 2007) (Figure 15). At lower mantle conditions the cubic phase is stabilized by anharmonic fluctuations, a picture confirmed by MD simulations (Li et al 2006a). This

behavior renders the QHA inadequate. High pressure and high temperature equation of state parameters and some thermoelastic properties have been obtained by MD (Li et al., 2006b) and by using a Landau potential with parameters determined by first-principles (Stixrude et al. 2007). This system still deserves to be further investigated by fully anharmonic techniques.

PHASE RELATIONS IN SILICATES AND OXIDES

The sharper discontinuities in the mantle are caused primarily by structural phase transformations in minerals. We have investigated systematically the ability of LDA and PBE-GGA exchange-correlation functionals combined with quasiharmonic free energy calculations to predict phase boundaries for polymorphic phase transitions and for one dissociation transition. The possible accuracy of such predictions was unclear. At phase boundary conditions bonds break and reconstruct, atoms may diffuse, phonons may become unstable, and other anharmonic effects may operate. Thermodynamic equilibrium between two phases is established by equating their Gibbs free energy, but these must be computed accurately. In general, large experimental hysteresis, indicates the existence of a large energy barrier along structural transformation paths. For these transformations, phonons are still quite stable and harmonic at phase boundary conditions. Therefore, the quasiharmonic free energy is expected to correctly describe phase boundary properties. But the QHA might not always be adequate. Even when it is, there are still uncertainties associated with the exchange-correlation functional that need to be assessed. Only a systematic approach can shed light on the limitations and uncertainties of each of these approximations. Although these approximations may generate large uncertainties for some properties, the uncertainties may be very small for others. Here we point out that broad trends can be extracted regarding the performance of these approximations for mantle silicates and oxides. We will also discuss below results of an anharmonic calculation of the forsterite to wadsleyite phase boundary (Wu and Wentzcovitch 2009).

Phase transitions in Mg_2SiO_4

Earth transition zone is characterized by the 410-km and 660-km seismic density and velocity discontinuities (see Fig. 1). The former can be accounted by the olivine to wadsleyite transition (α-to-β) and the latter is believed to be caused by the ringwoodite dissociation into ferripericlase and perovskite (γ-dissociation) (see Fig. 2). This transformation is also called the post-spinel transformation. Another less sharp discontinuity around 520-km depth may be caused by the wadsleyite to ringwoodite transition (β-to-γ). However, other interpretations for the 520 discontinuity also exist (Ita and Stixrude 1992, Saikia et al. 2008, Weidner and Wang 2000), such as $CaSiO_3$-perovskite ex-solution from the marjorite garnet solid solution. Over the past 40 years, starting from early experimental work by Ringwood and Major (1966), many efforts have been devoted to elucidating phase transitions in Mg_2SiO_4, including pinning down the exact phase boundary and their Clapeyron slopes. They have a significant impact on mantle convection models and on our understanding of this region. However, high *P-T in situ* experiments of phase boundary determination are challenging and there have been

uncertainties associated with measurements of pressure (pressure scales) and temperature at high pressures (pressure effect on thermocouple). It has been difficult to reach experimental consensus on Clapeyron slopes associated with the transitions expected at 410- and 660-km depths (see Fig. 16). Quasiharmonic first-principles calculations approach the problem from a different angle and avoid uncertainties intrinsic to measurements, such as reaction kinetics.

Systematic first-principles studies of the α-to-β-to-γ-to-pv+pc transitions in the Mg_2SiO_4-$MgSiO_3$-MgO system have been performed recently by Yu et al. (2006) and Yu et al. (2008). These calculations used the same set of parameters, including pseudopotentials and plane-wave kinetic energy cut-off. Results are documented and compared with high pressure experimental work and with density and bulk sound velocity discontinuity data in the mantle (Shearer and Flanagan 1999, Lawrence and Shearer 2006, Dziewonski and Anderson 1981). Owing to the intrinsic errors in currently available exchange-correlation functionals, the LDA and GGA phase boundaries bracket the experimentally determined ones with a common trend that the LDA underestimates the transition pressure by about 5 to 10 GPa, and the GGA overestimates it by up to ~3 GPa, irrespective of the transition pressure. The GGA phase boundary is somewhat closer to the experimental ones than the LDA.

Despite errors (or uncertainties) in the prediction of static transition pressures, the calculated Clapeyron slopes are essentially insensitive to the exchange-correlation functional used and are in quite good agreement with experimental measurements (see Table 2 and Fig. 16 and 17). Our calculations also agree with previous quasiharmonic calculations — 2.7 MPa/K (α–β transition) (Price et al. 1987, using inter-atomic potentials; Chopelas 1991, using measured zone center phonons) and 3.6 MPa/K (β–γ transition) (Pirce et al. 1987, 4.5 MPa/K). For the post-spinel transition the GGA phase boundary, including the Clapeyron slope, is closer to experimental results by Ito and Takahashi (1989) than to more recent *in situ* synchrotron X-ray data (Fei et al. 2004, Litasov et al. 2005). Nevertheless, calculations and experiments agree better at high temperature (above 1600^o C, Fig. 17) than at low temperature, suggesting that kinetics might be an issue in the experimental determinations of this dissociation phase boundary.

Mantle density discontinuities caused by phase transitions in Mg_2SiO_4

Despite the uncertainties in phase boundary determination, further analysis reveals that the calculated discontinuities in density, bulk modulus, and bulk sound velocity are quite insensitive to pressure and are useful to address the origin of different seismic discontinuities in the mantle, a much more complicated system with other co-existing phases. A discontinuity of a certain property across a phase transition can be defined as:

$$\frac{\Delta x}{x} = 2\left(\frac{x_B - x_A}{x_B + x_A}\right) \qquad (7)$$

with x being ρ, K_S, or V_Φ ($V_\Phi = \sqrt{K_S / \rho}$). Here A denotes the low-pressure phase and B the high-pressure phase. Results for ρ, K_S, and V_Φ, as well as these discontinuities ($\Delta x/x$) at 410-, 520-, 660-km conditions are shown in Table 2 together with seismic data and other mineral physics data. These results are shown also in Fig. 18. The lower (upper) bound of the shaded green bars is the discontinuity in a property calculated with the LDA (GGA) functional "along the GGA phase boundary", which is closer to the experimental ones. The solid lines in the middle of the green shaded regions show the average values. This comparison is made for sake of completeness only. Obviously, mantle discontinuities should be smaller since these transformations occur in aggregates rather than in pure end member minerals. However, the density discontinuity in the mantle produced by these single phase transformations can be estimated (Yu et al. 2006, Yu et al. 2009). If phase A transforms to A' in an aggregate of minerals consisting of phases A, B, C, etc, the density discontinuity produced is:

$$\frac{\Delta\rho}{\rho} = \frac{2y}{2/(1-\theta) - y} \tag{8}$$

where y is the volume fraction of phase A in the aggregate, e.g. ~60% of α, β, or γ in an aggregate with pyrolite composition (Ringwood 1979), and θ is the volume ratio of A' to A, which depends on the pressure and temperature at the transitions at 410-km, etc. For the α–β transition, θ= 0.9504, 0.9506, and 0.9509 (0.9444, 0.9446, and 0.9448) at 1300, 1500, and 1700 K along the GGA (LDA) boundary; for the β–γ transition, θ=0.9822, 0.9823, and 0.9824 (0.9796, 0.9797, and 0.9798) at 1500, 1700, and 1900 K along the GGA (LDA) boundary.

Using Eq. 8 and the calculated θ along the LDA and GGA phase boundaries, the density discontinuity versus the Mg_2SiO_4 volume fraction at 410-, 550-, and 660-km depth was computed using the LDA functional (Yu et al. 2006, Yu et al. 2008). The results are shown in Fig. 19c. According to the seismic impedance data of Shearer and Flanagan (1999), the density discontinuity at 660 km depth is ~5.2 %. Such density jump could be produced if the volume fraction of γ in the aggregate were ~67 %. This is close but slightly larger than the volume fraction of γ in an aggregate with pyrolite composition which is supposed to have ~60 vol% of γ. The larger density jump across the 660 discontinuity could have contributions from the garnet to perovskite transition which coexists with ringwoodite dissociation, but is known to be broader owing to Al effects (e.g. Ringwood 1975). The production of perovskite by the γ dissociation may alter the thermodynamic equilibrium of the garnet-perovskite system in favor of perovskite, which would also contribute to the density jump presumably (Weidner and Wang 2000).

For the 410-km, the large uncertainties in the seismic impedance data (~0.2--4%, Shearer and Flanagan 1999) prevent an unbiased conclusion about the volume fraction of forsterite or olivine (α) present at 410-km (Fig. 19a). Within this uncertainty it is safe to suggest that at most 80% of Mg_2SiO_4 is needed to produce the 410 discontinuity. The volume fraction in the pyrolite model, 60 vol.% would produce a density jump well within the range estimated from the impedance data. However, there could be other

factors contributing to the 410 discontinuity. At upper mantle conditions pyroxenes dissolve extensively into garnet over a large pressure range (~7–15 GPa at ~1200 °C). A drastic change in the proportion of pyroxene to garnet occurs near the end of the transformation (Ringwood, 1975; Akaogi and Akimoto, 1979; Irifune, 1987). This can produce a high velocity gradient between 300 and 460-km depth as pointed out by Ringwood (1975). The possibility that the pyroxene-to-garnet transformation coincides with the α–β transition in the mantle and contributes to the 410-km discontinuity is not excluded. In particular, Al, Ca, and Fe, affect phase equilibrium and the sharpness of the transitions in the pyroxene/garnet/Ca-pv system (solid-solid solution) (Stixrude 1997), but it still unclear how (e.g. Weidner and Wang 2000) and more mineral physics studies are needed.

The 520-km discontinuity is considerably weaker than the 410- or 660-km ones, and is also broader (~10-40 km). This discontinuity has been very debated because of controversial seismic observations coming from different schools using different types of seismic data, such as long or short period data, or reflection data at 520-km. Some found global or regional evidence of a 520-km discontinuity (e.g., Wiggins and Helmberger1973, Shearer 1990, Revenaugh and Jordan 1991, Ryberg et al. 1997), while others did not (Jones et al. 1992, Gossler and Kind 1996, Gu et al. 1998). Deuss and Woodhouse (2001) proposed a 520-km splitting into two discontinuities at 500-km and 560-km depth. Figure 19b compares the predicted density jump caused by the β-γ transition versus volume fraction of Mg_2SiO_4 in the aggregate, with the seismic observation by Lawrence and Shearer (2006). The best seismic estimate is 2.1±0.8%. This suggests that the volume fraction of Mg_2SiO_4 at 520-km is at least 70% (see Fig. 19b), which is excessive by any compositional model. Probably the pyroxene/garnet/Ca-pv system contributes to produce this discontinuity. There is evidence that Ca-pv ex-solves from garnet at ~1500 °C and 17–18 GPa (Gasparik 1989, Canil 1994) and can contribute to the discontinuity at 520-km depth (Weidner and Wang 2000, Saikia et al. 2008). These results verify that it is indispensable to include the impact of the pyroxene/garnet/Ca-pv system to understand the 520-km discontinuity, which presumably changes the width of this discontinuity as well.

Low pressure to high pressure $MgSiO_3$ clinoenstatite transition

Unlike reconstructive phase transitions such as the post-spinel transition, the low-pressure to high-pressure clinoenstatite transition in $MgSiO_3$ is a prototype of a displacive phase transition. As mentioned previously, Hp-En results when the lowest Ag displacement mode is superposed to the LP-En structure which is then relaxed. This transition is non-quenchable and reversible, with a large hysteresis in pressure (Angel and Hugh-Jones, 1994), which poses difficulties for experimental measurements. The calculated LDA and GGA phase boundaries for the LP-En-to-HP-En transition bracket the experimental hysteresis range and produce a 2.9 MPa/K Clapeyron slope (see Fig. 20). This provides useful information to constrain the LP-En, HP-En, and orthoenstatite triple point. These results suggest that the experimentally constrained triple point (Ulmer and Stalder, 2001) should be shifted up in pressure by 1 GPa (Yu et al. 2009).

Post-perovskite transition in $MgSiO_3$

The post-perovskite transition in $MgSiO_3$ (Murakami et al 2004, Tsuchiya et al 2004, Oganov and Ono 2004) is one of the most important findings in mineral physics since the discovery of the perovskite phase in 1974 (Liu 1974). Its geophysical implications are profound. Important new insights have been provided on the nature of the D" region with large lateral velocity variations and a clear discontinuity with wide topography varying from 0-300 km above the core mantle boundary. Previous experience with first-principles quasiharmonic phase boundary calculations was limited (Karki and Wentzcovitch 2003, Wentzcovitch et al. 2004) and the uncertainty of the predicted phase boundary for the post-perovskite transition was unclear (Tsuchiya et al 2004). The LDA and GGA phase boundaries are shown in Fig. 21. They differ by ~10 GPa. The Clapeyron slope obtained was 7.5 ± 0.3 MPa/K. At 125 GPa the transition temperature is very close to that observed by Murakami et al. (2004), 2,500 K. However, the experimental situation was very uncertain. An extensive review of experimental data on the post-perovskite transformation and on the properties of the post-perovskite phase was written by Hirose (2006). A detailed discussion of the experimental challenges associated with the determination of this phase boundary was presented. The main issue is the uncertainty in the pressure measurement owing to the discrepancies between various pressure markers, whether Pt (Holmes et al 1989), Au (Jamieson et al 1992, Tsuchiya 2003), or MgO (Speziale et al 2001). Using these markers the experimental Clapeyron slope varies from 5 to 11.5 MPa/K. Another first-principles calculation proposed a Clapeyron slope of 9.6-9.9 MPa/K (Oganov and Ono 2004).

This situation provided motivation for a systematic series of theoretical investigations of other phase transformations (Yu et al 2006, Yu et al 2008) that could be contrasted more clearly with experimental data. These studies helped to assert the calculated phase boundary for the post-perovskite transition (Tsuchiya et al 2004) and provided a concrete sense for the uncertainties involved. More recently, a highly engineered thermal equation of state for MgO combining anharmonic free energy calculations with experimental data (Wu et al 2008) was used to re-interpret experimental data. It produced a Clapeyron slope equal to 9.7 MPa/K. This latest value reduces the current discrepancy between theoretical calculations and experimental data. Anharmonic effects can still change the predicted Clapeyron slope. This phenomenon is discussed in the next section.

In the review on thermoelastic propeties of minerals (Wentzcovitch et al 2010) in this volume, an extensive discussion of this transformation and of the discontinuities in density and velocity it produces is given. Thermoelastic properties of this phase have been calculated using first-principles molecular dynamics(Stackhouse and Brodholt 2007). The influence of chemistry on this phase transformation has been investigated by first-principles (Caracas and Cohen 2007). The stability field of this phase, the search for post-post-perovskite polymorphs, and its dissociation into cotunnite-sype SiO2 and CsCl-type MgO at 11 Mbar has also been reviewed (Wentzcovitch et al 2007, Umemoto and Wentzcovitch 2010).

ANHARMONIC FREE ENERGY

The QHA does not account for anharmonic effects. In this approximation temperature effects on the crystal structure and on phonon frequencies are accounted by extrinsic volumetric effects only (quasiharmonic thermal expansivity). Because intrinsic temperature effects are more evident at high temperatures, the QHA becomes inadequate beyond a certain T located between the Debye temperature, θ_D, and the melting temperature, T_M (Matsui et al. 1994, Inbar and Cohen 1995, Wentzcovitch et al. 2004; Carrier et al., 2007). This effect is more visible at lower pressures. (see Fig. 8).

Several parameterizations for the anharmonic free energy have been proposed (Landau and Lifshitz 1980, Wallace 1972, Hui and Allen 1975, Gillet et al. 1999,Holzapfel et al. 2001, Oganov and Dorogokupets,. 2004) All these methods introduce inevitably volume-sensitive parameters or require explicit knowledge of the renormalized frequencies, none of which are easy to obtain at high pressures and temperatures. Recently, we proposed a semi-empirical parameterization (Wu and Wentzcovitch, 2009) that modifies the quasiharmonic phonon frequencies making them temperature dependent, $\Omega^F_{q,j}(V,T)$. These new frequencies can be used directly in the quasiharmonic free energy formula (Eq 9). $\Omega^F_{q,j}(V,T)$'s are not the renormalized frequencies $\Omega^S_{q,j}(V,T)$, which can only be used in the quasiharmonic entropy formula (Falk 1970, Wallace 1972, Hui and Allen 1975). Our parameterized phonon frequencies depend on a single parameter that is obtained by comparing predicted and measured thermodynamic properties:

$$\Omega^F_{q,j}(V,T) = \omega(V'), \tag{9}$$

with V':

$$V' = V\{1 - c\frac{[V - V_0]}{V_0}\} \tag{10}$$

V and V_0 are the predicted quasiharmonic volumes at high T and 0 K respectively, both at the same quasiharmonic pressure, $P(V,T)$. c is a constant to be determined empirically by using experimental thermodynamic data. This parameterization embodies the expected anharmonic behavior, which increases with temperature at constant pressure and decreases with pressure at constant temperature: V' tends to V at low temperatures and constant pressure or at high pressures and constant temperatures. Then, the anharmonic free energy is:

$$\begin{aligned} F_A(V,T) &= U(V) + \frac{1}{2}\sum_{q,j}\hbar\omega_{q,j}(V') + k_B T\sum_{q,j}\ln\{1 - \exp[-\hbar\omega_{q,j}(V')/k_B T] \\ &= U(V) + F_H(V',T) - U(V') \end{aligned} \tag{11}$$

The temperature dependence of Ω^F_i $(i \equiv q,j)$ can be expressed as (Wu and Wentzcovitch 2009):

$$a_i^F = \left(\frac{\partial \ln \Omega_i^F}{\partial T} \right)_V = \gamma_i(V')\alpha(V,T)c\beta \quad (12)$$

where $\beta = \frac{V^2 K_T}{V' V_0 K_0}, K_0, K_T$ are isothermal bulk moduli at 0 K and finite T, respectively, $\gamma_i(V')$ is the mode Grüneisen parameter, $\alpha(V,T)$ is the quasiharmonic thermal expansivity, and c is the empirically determined constant. At low temperatures, $\beta \sim 1$, a_i^F is proportional to $\alpha(V,T)$. At high temperature, the product $\beta\alpha(V,T)$ increases slightly and linearly with temperature. The temperature dependence of the Ω_i^F and the true renormalized frequencies, Ω_i^S is related approximately by (Wu and Wentzcovitch 2009):

$$a_i^S = \frac{\partial \ln \Omega_i^S}{\partial T} \approx (1+\eta_i) a_i^F \quad (13)$$

where $\eta_i = \frac{2k_B T}{h\Omega_i^F} - \exp(-\frac{h\Omega_i^F}{k_B T})(\frac{2k_B T}{h\Omega_i^F} + 1)$. η_i is positive and increases quickly with temperature if $k_B T < h\Omega_i^F$ and then tends to 1 when $k_B T > h\Omega_i^F$. Both η_i and the product $\beta\alpha$ from Eq. (12) increase rapidly with temperature at low temperatures and become weakly temperature dependent at high temperatures. Therefore we expect a noticeable nonlinearity in a_i^S at low temperatures and a nearly linear behavior at high temperatures. Such temperature behavior of the renormalized frequencies has been observed in diamond by Raman scattering (Zouboulis and Grimsditch, 1991; Anastassakis et al.; 1971). Equations (12) and (13) also show that the vibrational modes with smaller γ_i's have smaller a_i's in absolute values. This behavior of a_i's was indeed observed by Gillet et al. (1991). They found that the absolute value of a_i's for modes involving tetrahedral Si-O bond stretching with smaller γ_i's (Li et al 2007) are smaller than for other lattice modes.

As expected, at low temperatures anharmonic effects are negligible irrespective of c (see Fig. 22). Anharmonic effects also become less and less significant with increasing pressure and can be almost entirely overlooked up to 3,000 K at 100 GPa. This is consistent with conclusions by Inbar and Cohen (1995) obtained using the VIB method. The results show great improvement w.r.t. experimental thermodynamics data at high temperatures with increasing c. For c = 0.1, the predicted thermal expansivity differs from measured values by less than 1% up to the highest measured temperature, T = 1700 K at 0 GPa. γ_{th}, C_p, and K_S also show excellent agreement with experimental values (Isaak et al. 1989). Therefore, anharmonic effects described by Eq. (9-11) are very close to the expected one. This excellent agreement ensures that the pressure calibration based on P-V-T relations in MgO (Wu et al. 2008) derived using this anharmonic free energy have very precise thermal pressure. The property most affected by anharmonicity is the thermal expansivity, α, followed by γ_{th} and C_P, with K_S being the least sensitive (see

Table 4). At conditions of the uppermost lower mantle anharmonicity changes the quasiharmonic K_S of MgO by 0.8%. Anharmonicity decreases with increasing pressure and at core-mantle-boundary conditions the anharmonic contribution to the K_S of MgO is only -0.09%. At the transition zone conditions anharmonicity changes the quasiharmonic K_S of forsterite and wadsleyite by less than 0.5%.

One naturally suspects that anharmonicity might be significant at phase boundaries. Their precise determination is necessary to constrain the thermal structure and mineralogy of the mantle. The forsterite to wadsleyite transition, which is responsible for seismic velocity discontinuities around 410 km depth, is a good test case for a couple of reasons: i) there are discrepancies between predicted and measured Clapeyron slopes (CS). All calculations used the QHA and predict similar values (see Table 5); ii) anharmonic effects have long been recognized in forsterite since its heat capacity at constant volume, C_v, can exceed the Dulong-Petit limit at high temperature (Cynn et al. 1996, Anderson et al. 1991 Gillet et al 1991, Bouhifd et al 1996); iii) it has been recognized that the conditions at the 410 km discontinuity is at the borderline limit of validity of the QHA (Li et al. 2007,Yu et al. 2008). Therefore, anharmonicity could be the source of the discrepancy between quasiharmonic predictions and measured or semi-empirical CS's.

We find that anharmonic effects are opposite in forsterite and wadsleyite and this enhances anharmonic effects on their phase boundary (Wu and Wentzcovitch, 2009). The parameter c for forsterite is ~ -0.06. This was determined by matching predicted and experimental C_p's since this is most consistent experimental thermodynamics data (see Fig. 23a). The anharmonic correction considerably improves the predicted heat capacity (see Fig 23a for C_p) and thermal expansivity (Matsui and Manghnani, 1985; Suzuki et al., 1984; Wu and Wentzcovitch, 2009). Anharmonic corrections with c= -0.06 raise C_v beyond the Dulong-Petit limit at ~2000 K. The experimental crossing temperatures are 1300 ~ 1500 K (Cynn et al. 1996, Anderson et al. 1991 Gillet et al 1991, Bouhifd et al 1996). It appears that differences in the crossing temperatures are mainly caused by thermal expansion data used to calculate C_v (C_p/[1+$\alpha\gamma_{th}T$]). The thermal expansivity data adopted in these experiments are much smaller than Matsui and Manghnani's (1985) and Suzuki et al.'s (1984). The parameter c for wadsleyite is ~0.08. This was determined by direct comparison of predicted and experimental thermal expansivity (Suzuki et al., 1984) (see Fig. 23b).

The anharmonic contribution to the free energy is negative for forsterite and positive for wadeleyite. This leads to anharmonic stabilization of forsterite at high temperatures. As shown in Fig. 24, $c_\alpha = -0.06$ and $c_\beta = 0.08$ increase the transformation pressure by ~1 GPa at 1700 K and the CS increases from 2.7 MPa/K ($c_\alpha = c_\beta = 0$) to 3.6 MPa/K (Wu and Wentzcovitch, 2009) We also found that, at 1700 K, the CS varies quite linearly with c_α and c_β and can be expressed as: $CS = CS_0 + 7.82(c_\beta - c_\alpha)$, where CS_0 is the slope given by a quasiharmonic calculation ($c_\alpha = c_\beta = 0$). Therefore, anharmonicity may affect the CS particularly strongly when one phase has positive c and the other phase has negative c. In the present case, the discrepancy between direct measurements and calculations of the CS is reconciled after inclusion of anharmonicity in the calculations (see table 5).

Finally, we found that this parameterization reproduces the correct high and low temperature behaviors of the anharmonic free energy (Wu and Wentzcovitch, 2009). Anharmonic free energy can be well fitted by T^2 at high temperature and exhibit the typical T^4 behavior at low temperature for MgO, forsterite and wadsleyite.

SUMMARY

Quasiharmonic theory combined with first-principles phonon density of states gives accurate thermodynamics properties of minerals at the high pressures and temperatures of the Earth interior. Care must be exercised in using this method within its regime of validity. A simple criterion to establish the approximate upper temperature limit of validity of the QHA versus pressure was introduced based on *a posteriori* inspection of the thermal expansivity. This criterion shows that the QHA is a good approximation for minerals at mantle conditions, except for truly anharmonic crystals like $CaSiO_3$-perovskite, and perhaps for minerals at conditions of the core-mantle boundary. In general, the temperature range of applicability of the QHA increases with pressure.

The systems analyzed here, were all investigated consistently and systematically, using the same pseudopotentials, convergence criteria, plane-wave cut-offs, and *k*- and *q*-point samplings in LDA and PBE-GGA calculations. The trends extracted from these calculations are therefore reliable. The importance of zero-point-motion effects on structural properties cannot be overemphasized. The LDA exchange-correlation functional gives considerably superior results for 0 K properties after the zero-point-motion energy is included in the calculation. GGA results consistently overestimate volume and underestimate the bulk modulus by several percent. LDA thermodynamic properties at ambient conditions are in excellent agreement with experimental values.

The performance of these exchange-correlation functionals was also investigated for predictions of thermodynamic phase boundaries. In general, the LDA phase boundaries are "shifted" by 5-10 GPa to lower pressures compared to the experimental ones, while GGA boundary are closer to experimental ones but still "shifted" by 2-5 GPa to higher pressures. LDA and GGA Clapeyron slopes are very similar and in fairly good agreement with experimental slopes. Phase boundaries, however, may be more affected by anharmonicity since bond-breaking and bond-reconstruction, phonon softening, diffusion, etc may take place at these pressures and temperatures.

Discontinuities in density and bulk sound velocity for important phase transformations in the mantle transition zone were systematically investigated. Only the magnesium end-members, Mg_2SiO_4, were studied. Predicted discontinuities in density, bulk modulus, and bulk sound velocity are sharp and have useful accuracy for analysis of mantle discontinuities, despite uncertainties in the predicted phase boundary. With the rough premise that the olivine system does not interact with other minerals such as pyroxene/garnet/Ca-perovskite, we were able estimate density discontinuities at 410-km, 520-km, and 660-km depth and compare them with those inferred from seismic data. We

conclude that seismic density discontinuities observed at 410-km (0.2-4%) and 660-km (~5.2%) depth can be produced by phase transition in the olivine system alone in a mantle with pyrolite composition (~60 vol% olivine). However, the 520-km discontinuity (2.1±0.8%) cannot. It requires contributions from other mantle transformations, e.g., the Ca-perovskite ex-solution from majorite garnet. We also discuss the post-perovksite phase boundary. Our predicted Clapeyron slope, ~7.5±0.3 MPa/K, differs somewhat from the preferred experimental slopes, > 9.7 MPa/K. This suggests that this phase boundary might be sensitive to anharmonic effects.

We have introduced a semi-empirical *ansatz* to compute anharmonic contributions to the free energy. This method utilizes experimental data at low pressures and high temperatures on *one* property, preferably thermal expansivity, to compute *all* thermodynamic properties at high pressures and high temperatures. It offered excellent results for MgO, and the P-V-T relation in this mineral was offered for pressure calibration in diamond-anvil-cells experiments. It was also applied to foresterite (α), wadsleyite (β), and to the α-to-β transformation. The thermodynamic properties of the α- and β-phases improve and are futher reconciled with experimental measurements beyond the QHA validity regime after correction for anharmonic effects. This study indicated that anhamonicity manifests differently in different systems, depending whether the "average" phonon frequency increases (β and MgO) or decreases (α) with temperature at constant volume. This difference in behavior affects the Clapeyron slope of the α-to-β transformation, raising it from 2.5-2.6 to 3.6 MPa/K and reconciling it with the latest experimental determinations. Anharmonic effects are most evident in the thermal expansity, followed by the thermal Grüneisen parameter, constant pressure specific heat, and least evident in the bulk modulus.

APPENDIX

Pseudopotentials used here are the same as those used in Tsuchiya et al. 2004. Pseudopotentials for oxygen and silicon were generated by Troullier and Martins method (Troullier and Martins 1993) and that of magnesium was generated by the method of von Barth and Car (von Barth and Car, unpublished). For O, the reference configuration is $2s^2 2p^4$, r_s and r_p are both 1.45 a.u. p-local; for Si, $3s^2 3p^2 3d^0$, $r_s=r_p=r_d=1.47$ a.u. d-local. Mg pseudopotential was generated from five configurations, $3s^2 3p^0$, $3s^1 3p^1$, $3s^1 3p^{0.5} 3d^{0.5}$, $3s^1 3p^{0.5}$, $3s^1 3d^1$ with decreasing weights 1.5, 0.6, 0.3, 0.3, and 0.2, respectively, $r_s=r_p=r_d=2.5$ a.u. d-local, nonlinear core correction (Louie et al. 1982) was used.

We have used the same plane-wave energy cut off, 70 Ry, and the same criterion for *k*-point sampling convergence, 5×10^{-5} Ry/atom. The Monkhost-Pack *k*-point mesh adopted in these calculations were 4×4×4, 4×2×4, 4×4×4, 4×4×4, 6×6×4, 4×4×8, 4×4×4, 4×4×4, 4×4×4, and 2×2×2 with a 1/2 shift from the origin for MgO, foresterite wadsleyite, wadsleyite, ringwoodite, post-perovskite, stishovite, LP-enstatite, HP-enstatite, ilmenite, and majorite, respectively. Structure optimizations were performed using variable cell shape MD (Wentzcovtich 1991). Phonons were directly calculated (Baroni et al 2000) on 2×2×2 *q*-point and then interpolated for denser meshes to calculate phonon dispersions and density of states. Results on perovskite are from Tsuchiya et al.

(2005) where equivalent parameters were used. All calculations were performed in primitive cells (not unit cell in general) using the Quantum ESPRESSO distribution (Gianozzi et al 2009).

ACKNOWLEDGEMENT

This research was supported by NSF grants EAR 0810272, EAR 0635990, ATM 0428774 (VLab), EAR 0757903.

REFERENCES

Akaogi M, Akimoto S (1979) High-pressure phase equilibria in a garnet lherzolite, with special reference to Mg^{2+}–Fe^{2+} partitioning among constituent minerals. Phys Earth Planet Inter 19: 31–51

Adams DJ, Oganov AR (2006) Ab initio molecular dynamics study of $CaSiO_3$ perovskite at P-T conditions of Earth's lower mantle. Phys Rev B 73: 184106.

Akaogi M, Ito E, Navrotsky A (1989) Olivine-modified spinel-spinel transitions in the system Mg_2SiO_4–Fe_2SiO_4: Calorimetric measurements, thermochemical calculation, and geophysical application. J Geophys Res 94: 15,671–15,685

Akaogi M, Yano M, Tejima Y, Iijima M, Kojitani H (2004) High-pressure transitions of diopside and wollastonite: phase equilibria and thermochemistry of $CaMgSi_2O_6$, $CaSiO_3$ and $CaSi_2O_5$–$CaTiSiO_5$ system Phys Earth Planet Inter 143-144: 145-156

Akaogi M, Yusa H, Shiraishi K, Suzuki T (1995) Thermodynamic properties of α-quartz, coesite, and stishovite and equilibrium phase relations at high pressures and high temperatures. J Geophys Res100: 22337–22348

Anastassakis E, Hwang HC, Perry CH (1971) Temperature dependence of the long-wavelength optical phonons in diamond. Phys. Rev. B 4: 2493-2497

Anderson OL, Isaak DL, Oda H (1991) Thermoelastic parameters for six minerals at high temperature. J Geophys Res 96:18037-18046

Andrault D, Angel RJ, Mosenfelder JL, Le Bihan T (2003) Equation of state of stishovite to lower mantle pressures. Am Mineral 88: 301–307

Angel RJ, Finger LW, Hazen RM, Kanzaki M, Weidner DJ, Leibermann RC, Veblen DR (1989) Structure and twinning of single-crystal $MgSiO_3$ garnet synthesized at 17 GPa and 1800◦ C. Am Mineral 74: 509–512

Angel RJ, Hugh-Jones DA (1994) Equations of state and thermodynamic properties of enstatite pyroxenes. J Geophys Res 99: 19777–19783

Anisimov VI, Zaanen J, Andersen OK (1991) Band theory and mott insulators: Hubbard u instead of stoner I. Phys Rev B 44: 943–954

Ashida T, Kume S, EI (1987) Thermodynamic aspects of phase boundary among α-, β-, and γ- Mg_2SiO_4. In High Pressure Research in Mineral Physics, Manghnani M, Syono Y, eds. Geophysical Monograph 39, American Geophysical Union, 269–274

Baroni S, de Gironcoli S, Corso AD, Giannozzi P (2001) Phonons and related crystal properties from density-functional perturbation theory. Rev Mod Phys 73: 515–562

Berman RG, Brown TH (1985) Heat capacity of minerals in the system Na_2O-K_2O-CaO-MgO-FeO-Fe_2O_3-Al_2O_3-SiO_2-TiO_2-H_2O-CO_2. Contrib Mineral Petrol 89:168-183 14

Bonini N, Lazzeri M, Marzari N Mauri F (2007) Phonon anharmonicities in graphite and graphene. Phys Rev Lett 99: 176802

Bertheville B, Bill H, Hagemann, H (1998) Experimental Raman scattering investigation of phonon anharmonicity effects in Li_2S. J Phys: Condens Matter 10: 2155-2169

Boehler R (2000) High-pressure experiments and the phase diagram of lower mantle and core materials. Rev Geophys 38: 221–246

Boehler R, Ross M (1997) Melting curve of aluminum in a diamond cell to 0.8 Mbar: implications for iron. Earth Planet Sci Lett 153: 223–227

Born M, Huang K (1956) Dynamical theory of crystal lattices. International series of monographs on physics. Oxford at the Clarendon Press, Hong Kong

Bouhifd MA, Andrault D, Fiquet G, Richet P (1996) Thermal expansion of forsterite up to the melting point. Geophys Res Lett 23: 1143–1146

Brown JM, Shankland TJ (1981) Thermodynamic parameters in the Earth as determined from seismic profiles. Geophys J International 66: 579–596

Canil D (1994) Stability of clinopyroxene at pressure–temperature conditions of the transition region. Phys Earth Planet Inter 86: 25–34

Caracas R, Wentzcovitch RM, Price GD, and Brodholt J (2005) CaSiO3 perovskite at lower mantle pressures, Geohys Res Lett 144:L06306.

Caracas R and Wentzcovitch RM (2006) Theoretical determination of the structures of $CaSiO_3$ perovskites, Acta Crystallogr B 62: 1025-1030.

Caracas R Cohen R (2007) The effect of chemistry on the physical properties of perovskite and post-perovskite, ed by Hirose K, Brodholt J, Lay T, Yuen D, Post-perovskite, The last mantle phase transition, AGU Monograph Series 174:115-128.

Carrier P, Wentzcovitch R, Tsuchiya J (2007) First-principles prediction of crystal structures at high temperatures using the quasiharmonic approximation. Phys Rev B 76: 064116

Carrier P, Justo JF, Wentzcovitch RM (2008) Quasiharmonic elastic constants corrected for deviatoric thermal stresses. Phys Rev B 78: 144302

Ceperley DM, Alder BJ (1980) Ground state of the electron gas by a stochastic method. Phys Rev Lett 45: 566–569

Chopelas A (1990) Thermal properties of forsterite at mantle pressure derived from vibrational spectroscopy. Phys Chem Miner 17: 149–156

Chopelas A (1991) Thermal properties of β-Mg2SiO4 at mantle pressures derived from vibrational spectroscopy: Implications for the mantle at 400 km depth. J Geophys Res 96: 11817–11829

Chopelas A (1996) Thermal expansivity of lower mantle phases MgO and $MgSiO_3$ perovskite at high pressure derived from vibrational spectroscopy. Phys Earth Planet Inter 98: 3–15

Chopelas A (1999) Estimates of mantle relevant Clapeyron slopes in the $MgSiO_3$ system from highpressure spectroscopic data. Am Mineral 84: 233–244

Chopelas A (2000) Thermal expansivity of mantle relevant magnesium silicates derived from vibrational spectroscopy at high pressure. Am Mineral 85: 270–278

Chopelas A, Boehler R, Ko T (1994) Thermodynamics and behavior of -Mg_2SiO_4 at high-pressure: Implications for Mg_2SiO_4 phase equilibrium. Phys Chem Mineral 21: 351–359

Cococcioni M, de Gironcoli S (2005) Linear response approach to the calculation of the effective interaction parameters in the LDA+U method. Phys Rev B 71: 035105

Cynn H, Carnes JD, Anderson OL (1996) Thermal properties of forsterite, including C_v, calculated from αKT through the entropy. J Phys Chem Solids 57:1593-1599

da Silva C, Stixrude L, Wentzcovitch RM (1997) Elastic constants and anisotropy of forsterite at high pressure. Geophys Res Lett 24: 1963–1966.

Deuss A, Woodhouse J (2001) Seismic observations of splitting of the Mid-Transition Zone discontinuity in Earth's mantle. Science 294: 354–357.

Downs JW, Bukowinski MST (1997) Variationally induced breathing equations of state of pyrope, grossular, and majorite garnets. Geophys Res Lett 24: 1959–1962

Downs RT, Zha CS, Duffy TS, Finger LW (1996) The equation of state of forsterite to 17.2 GPa and effects of pressure media. Am Mineral 81: 51–55

Duan W, Karki BB, Wentzcovitch RM, and Gu BL (2001) Crystal chemistry of $MgSiO_3$ low-clinoenstatite. Am Mineral 86: 762

Durben DJ, Wolf GH (1992) High-temperature behavior of metastable MgSiO3 perovskite: a Raman spectroscopic study. Am Mineral 77: 890–893

Dziewonski AM, Anderson DL (1981) Preliminary reference Earth model. Phys Earth Planet Inter 25: 297–356

Falk H (1970) Inequalities of J. W. Gibbs. J Phys 38: 858–869

Fei Y (1999) Effects of temperature and composition on the bulk modulus of (Mg, Fe) O. Am Mineral 84: 272–276

Fei Y, Van Orman J, Li J, van Westrenen W, Sanloup C, Minarik W, Hirose K, Komabayashi T, Walter M, Funakoshi K (2004) Experimentally determined postspinel transformation boundary in Mg_2SiO_4 using MgO as an internal pressure standard and its geophysical implications. J Geophys Res 109: 2305

Feldman JL, Horton GK, Lurie JB (1965) A one-parameter treatment of anharmonic specific heat. J Phys Chem Solids, 26: 1507–1516

Foiles SM (1994) Evaluation of harmonic methods for calculating the free energy of defects in solids. Phys Rev B 49: 14930–14938

Gasparik T (1989) Transformation of enstatite–diopside–jadeite pyroxenes to garnet. Contrib Mineral Petrol 102:389–405

Gasparik T (1990) Phase relations in the transition zone. J Geophys Res 95: 15751–15769

Gerald Pacalo RE, Weidner DJ (1997) Elasticity of majorite, $MgSiO_3$ tetragonal garnet. Phys Earth Planet Inter 99: 145–154

Giannozzi P et al (2009) QUANTUM ESPRESSO: a modular and open-source software project for quantum simulations of materials. J Phys Condens Matter 21:395502.

Gillet P, Matas J, Guyot F, Ricard Y (1999) in Thermodynamic properties of minerals at high pressures and temperatures from vibrational spectroscopic data, microscopic properties and processes in minerals, edited by Wright K, Catlow R, NATO Advanced Studies Institute, Series C: mathematical and physical sciences (Kluwer, Dordrecht), 543: 71–92.

Gillet P, Richet P, Guyot F, Fiquet G (1991) High-temperature thermodynamic properties of forsterite. J Geophys Res 96: 11805–11816

Gossler J Kind R (1996) Seismic evidence for very deep roots of continents. Earth Planet Sci Lett 138: 1–13

Gu Y, Dziewonski A, Agee C (1998) Global de-correlation of the topography of transition zone discontinuities. Earth Planet Sci Lett 157: 57–67

Guyot F, Yanbin W, Gillet P, Ricard Y (1996) Quasi-harmonic computations of thermodynamic parameters of olivines at high-pressure and high-temperature. A comparison with experiment data. Phys Earth Planet Inter 98: 17–29

Hamann D, Schluter M, Chiang C (1979) Norm-Conserving Pseudopotentials. Phys Rev Lett 43: 1494–1497

Hazen RM,WeinbergerMB, Yang H, Prewitt CT (2000) Comparative high-pressure crystal chemistry of wadsleyite, β-$(Mg_{1-x}Fe_x)_2SiO_4$ with x= 0 and 0.25. Am Mineral 85: 770–777

Hazen RM, Zhang J, Ko J (1990) Effects of Fe/Mg on the compressibility of synthetic wadsleyite: β-$(Mg_{1-x}Fe_x)_2SiO_4$ ($x \leq 0.25$). Phys Chem Miner 17: 416–419

Hirose K (2006) Postperovskite phase transition and its geophysical implications. Rev Geophys 44: 3001

Hohenberg P and Kohn W (1964) Inhomogeneous electron gas. Phys Rev 136: 864-871

Holland KG and Ahrens TJ (1997) melting of $(Mg,Fe)SiO_4$ at the core mantle boundary of the Earth. Science 275: 1623-1625

Holmes NC, Moriarty JA, Gathers GR, Nellis WJ (1989) The equation of state of platinum to 660 GPa (6.6 MBar). J Appl Phys 66: 2962–2967

Holzapfel WB, Hartwig M, Sievers W (2001) Equations of state for Cu, Ag, and Au for wide ranges in temperature and pressure up to 500 GPa and Above. J Phys Chem Ref Data 30: 515-528

Horiuchi H, Hirono M, Ito E, Matsui Y (1982) $MgSiO_3$ (ilmenite-type): single crystal X-ray diffraction study. Am Mineral 67: 788–793

Horiuchi H, Sawamoto H (2000) β--Mg_2SiO_4: Single-crystal X-ray diffraction study. Am Mineral 66: 568–575

Hui JCK, Allen PB (1975) Thermodynamics of anharmonic crystals with application to Nb. J Phys C: Solid State Phys 8: 2923-2935.

Inbar I, Cohen RE (1995) High pressure effects on thermal properties of MgO. Geophys Rev Lett 22: 1533-1536.

Inoue T, Irifune T, Higo Y, Sanehira T, Sueda Y, Yamada A, Shinmei T, Yamazaki D, Ando J, Funakoshi K, UtsumiW(2006) The phase boundary between wadsleyite and ringwoodite in Mg_2SiO_4 determined by in situ X-ray diffraction. Phys Chem Miner 33: 106–114

Irifune T (1987) An experimental investigation of the pyroxene-garnet transformation in a pyrolite composition and its bearing on the constitution of the mantle. Phys Earth Planet Inter 45: 324–336

Irifune T, Nishiyama N, Kuroda K, Inoue T, Isshiki M, Utsumi W, Funakoshi K, Urakawa S, Uchida T, Katsura T, Ohtaka O (1998) The Postspinel Phase Boundary in Mg_2SiO_4 Determined by in Situ X-ray Diffraction. Science 279: 1698–1700

Isaak DG, Anderson OL, Goto T (1989) Measured elastic moduli of single-crystal MgO up to 1800 K. Phys Chem Miner 16: 704–713

Ita J, Stixrude L (1992) Petrology, elasticity, and composition of the mantle transition zone. J Geophys Res 97: 6849–6866

Ito E, Takahashi E (1989) Postspinel transformations in the system Mg_2SiO_4–Fe_2SiO_4 and some geophysical implications. J Geophys Res 94: 10637–10646

E. Ito and H. Yamada (1982) Stability relations of silicate spinels, ilmenites and perovskites .In High Pressure Research in Mineral Physics, Akamoto S, Manghnani MH, eds, Center for Academic Publishing of Japan, 405–419

Jackson J, Sinogeikin SV, Bass J (2000) Sound velocities and elastic properties of γ-Mg_2SiO_4 to 873 K by Brillouin spectroscopy. Am Mineral 85: 296–303

Jamieson JC, Fritz JN, Manghnani MH (1982) Pressure measurement at high temperature in x-ray diffraction studies: Gold as a primary standard, in High-Pressure Research in Geophysics, edited by S. Akimoto and M. H. Manghnani. Adv Earth Planet Sci 12: 27–48

Jeanloz R, Ahrens T, Mao HK, Bell PM (1979) B1-B2 transition in calcium oxide from shock-wave and diamond-cell experiments, Science 206: 829-831

Jones LE, Mori J, Helmberger DV (1992) Short-period constraints on the proposed transition zone discontinuity. J Geophys Res 97: 8765–8774

Karki BB, Wentzcovitch RM (2002) First-principles lattice dynamics and thermoelasticity of $MgSiO_3$ ilmenite at high pressure. J Geophy Res 107: 2267

Karki BB, Wentzcovitch RM (2003) Vibrational and quasiharmonic thermal properties of CaO under pressure. Phys Rev B 68: 224304

Karki BB, Wentzcovitch RM, de Gironcoli S, Baroni S (1999) First-principles determination of elastic anisotropy and wave velocities of MgO at lower mantle conditions. Science 286: 1705–1707

Karki BB, Wentzcovitch RM, de Gironcoli S, Baroni S (2000a) High-pressure lattice dynamics and thermoelasticity of MgO. Phys Rev B 61: 8793–8800

Karki BB, Wentzcovitch RM, de Gironcoli S, Baroni S (2000b) Ab initio lattice dynamics of $MgSiO_3$ perovskite at high pressure. Phys Rev B 62: 14750–14756

Katsura T, Ito E (1989) The system Mg_2SiO_4–Fe_2SiO_4 at high pressures and temperatures: Precise determination of stabilities of olivine, modified spinel, and spinel. J Geophys Res 94: 15663–15670

Katsura T, Yamada H, Nishikawa O, Song M, Kubo A, Shinmei T, Yokoshi S, Aizawa Y, Yoshino T, Walter MJ, Ito E, Funakoshi Ki (2004a) Olivine-wadsleyite transition in the system $(Mg,Fe)_2SiO_4$. J Geophys Res 109: 2209

Katsura T, Yamada H, Shinmei T, Kubo A, Ono S, Kanzaki M, Yoneda A,Walter MJ, Ito E, Urakawa S, Funakoshi K, Utsumi W (2003) Post-spinel transition in Mg_2SiO_4 determined by high P-T in situ X-ray diffractometry. Phys Earth Planet Inter 136: 11–24

Katsura T, Yokoshi S, Song M, Kawabe K, Tsujimura T, Kubo A, Ito E, Tange Y, Tomioka N, Saito K, Nozawa A, Funakoshi Ki (2004b) Thermal expansion of ringwoodite at high pressures. J Geophys Res 109: B12209

Kennett BLN, Engdahl ER, Buland R (1995) Constraints on seismic velocities in the Earth from travel-times. Geophys. J. Int. 122, 108-124.

Kiefer B, Stixrude L, Wentzcovitch RM (1997) Elastic constants and anisotropy of Mg_2SiO_4 spinal at high pressure. Geophys Res Lett 24: 2841-2844

Knittle E, Jeanloz R, Smith GL (1986) Thermal expansion of silicate perovskite and stratification of the earth's mantle. Nature 319: 214–216

Kohn W, Sham LJ (1965) Self-Consistent Equations Including Exchange and Correlation Effects. Phys Rev 140: 1133–1138

Komabayashi T, Hirose K, Sugimura E, Sata N, Ohishi Y, Dubrovinsky LS (2008) Simultaneous volume measurements of post-perovskite and perovskite in $MgSiO_3$ and their thermal equations of state. Earth Planet Sci Lett 265: 515–524

Kurashina T, Hirose K, Ono S, Sata N, Ohishi Y (2004) Phase transition in Al-bearing $CaSiO_3$ perovskite: implications for seismic discontinuities in the lower mantle. Phys Earth Planet Inter 145: 67-74

Landau LD, Lifshitz EM Course of theoretical physics, statistical physics, Part I (Butterworth & Heinemann: Oxford, 1980) Vol. 5

Lawrence JF, Shearer PM (2006) Constraining seismic velocity and density for the mantle transition zone with reflected and transmitted waveforms. Geochem Geophys Geosyst 7: Q10012

Lazzeri M, Calandra M, Mauri F (2003) Anharmonic phonon frequency shift in MgB_2. Phys Rev B 68: 220509

Li B (2003) Compressional and shear wave velocities of ringwoodite -Mg_2SiO_4 to 12 GPa. Am Mineral 88: 1312–1317

Li L, Weidner D, Brodholt J, Alfe D, Price GD, Caracas R, Wentzcovitch R (2006a) Elasticity of $CaSiO_3$ perovskite at high pressure and high temperature, Phys Earth Planet Int 155: 249-259

Li L, Weidner D, Brodholt J, Alfe D, Price GD, Caracas R, Wentzcovitch R (2006b) Phase stability of $CaSiO_3$ perovskite at high pressure and high temperature: insights from ab initio molecular dynamics, Phys Earth Planet Int 155: 260-268

Li L, Wentzcovitch RM, Weidner DJ, Da Silva CRS (2007) Vibrational and thermodynamic properties of forsterite at mantle conditions. J Geophys Res 112: B05206

Li L, Weidner DJ, Brodholt J, Alfè D, Price GD, (2006b) Elasticity of Mg2SiO4 ringwoodite at mantle conditions, Phys Earth Planet Int 157: 181-187

Li L, Weidner DJ, Brodholt J, Alfè D, Price GD (2009) Ab initio molecular dynamics study of elasticity of akimotoite MgSiO3 at mantle conditions, Phys Earth Planet Int 173: 115-120

Li L, Weidner DJ, Brodholt J, Price GD (2007) The effect of cation-ordering on the elastic properties of majorite: An ab initio study, Earth Planet Sc Lett 256: 28-35

Litasov K, Ohtani E, Sano A, Suzuki A, Funakoshi K (2005) In situ X-ray diffraction study of postspinel transformation in a peridotite mantle: Implication for the 660-km discontinuity. Earth Planet Sci Lett 238: 311–328

Liu L-G (1974) Silicate perovskite from phase transformations of pyrope-garnet at high pressure and temperature, Geophys Res Lett 1: 277–280.

Liu L-G (1975) Post-oxide phases of forsterite and enstatite. Geophys Res Lett 2: 417–419

Liu L-G (1977) First Occurrence of the Garnet-Ilmenite Transition in Silicates. Science 195: 990 – 991

Louie SG, Froyen S, Cohen ML (1982) Nonlinear ionic pseudopotentials in spin-density-functional calculations. Phys Rev B 26:1738–1742

Lu R, Hofmeister AM (1994) Infrared-spectroscopy of CaGeO3 perovskite to 24-GPa and thermodynamic implications. Phys Chem Miner 21: 78–84

Lu R, Hofmeister AM, Wang Y (1994) Thermodynamic properties of ferromagnesium silicate perovskites from vibrational spectroscopy. J Geophys Res 99: 11795–11804

Mao HK, Hemley RJ, Fei Y, Shu JF, Chen LC, Jephcoat AP,Wu Y, BassettWA (1991) Effect of pressure, temperature, and composition on lattice parameters and density of (Fe,Mg)SiO_3-perovskites to 30 GPa. J Geophys Res 96: 8069–8079

Matsui T, Manghnani MH (1985) thermal expansion of single-crystal forsterite to 1023 K by Fizeau interferometry. Phys Chem Minerals 12: 201-210

Matsui M, Price GD, Patel A (1994) Comparison between the lattice dynamics and molecular dynamics methods: Calculation results for $MgSiO_3$ perovskite. Geophys Rev Lett 21: 1659-1662

Meng Y, Fei Y, Weidner DJ, Gwanmesia GD, Hu J (1994) Hydrostatic compression of -Mg_2SiO_4 to mantle pressures and 700 K: Thermal equation of state and related thermoelastic properties. Phys Chem Miner 21: 407–412

Morishima H, Kato T, Suto M, Ohtani E, Urakawa S, Utsumi W, Shimomura O, Kikegawa T (1994) The Phase Boundary Between α- and β-Mg_2SiO_4 Determined by in Situ X-ray Observation. Science 265: 1202–1203

Murakami M, Hirose K, Kawamura K, Sata N, Ohishi Y (2004) Post-Perovskite Phase Transition in $MgSiO_3$. Science 304: 855–858

Oda H, Anderson OL, Isaak DG, Suzuki I (1992) Measuremens of elastic properties of single-crystal CaO up to 1200 K, Phys Chen Miner 19:96-105

Oganov AR, Brodholt JP, Price GD (2001) The elastic constant of $MgSiO_3$ perovskite at pressure and temperatures of the Earth's mantle. Nature 411:934-937

Oganov AR, Dorogokupets PI (2004) Intrinsic anharmonicity in equations of state and thermodynamics of solids. J Phys: Condens Matter 16: 1351-1360

Oganov AR, Gillan MJ, Price GD (2005) Structural stability of silica at high pressures and temperatures. Phys Rev B 71: 064104

Oganov AR, Ono S (2004) Theoretical and experimental evidence for a post-perovskite phase of $MgSiO_3$ in Earth's D" layer. Nature 430: 445–448

Ono S, Oganov AR (2005) In situ observations of phase transition between perovskite and $CaIrO_3$-type phase in $MgSiO_3$ and pyrolitic mantle composition. Earth Planet Sci Lett 236: 914– 932

Ono S, Ohishi Y, Mibe K, (2004) Phase transition of Ca-perovskite and stability of Al-bearing Mg-perovskite in the lower mantle. Am Mineral 89: 1480

Orr RL (1953) High temperature heat contents of magnesium orthosilicate and ferrous orthosilicate. J Am Chem Soc 75: 528-529

Overton WC (1968) An analysis of the cubic contributions to the anharmonic frequency shift and free energy for bravais crystals. J Phys Chem Solids 29: 711-718

Parrinello M, Rahman A (1980) Crystal structure and pair potentials: A molecular-dynamics study. Phys Rev Lett 45: 1196

Perdew J, Zunger A (1981) Self-interaction correction to density-functional approximations formanyelectron systems. Phys Rev B 23: 5048–5079

Perdew JP, Burke K, Ernzerhof M (1996) Generalized Gradient Approximation Made Simple. Phys Rev Lett 77: 3865–3868

Piekarz P, Jochym PT, Parlinski K, Lazewski J (2002) Highpressure and thermal properties of γ-Mg_2SiO_4 from first-principles calculations. J Chem Phys 117: 3340–3344

Price GD, Parker SC, Leslie M (1987) The lattice dynamics and thermodynamics of the Mg_2SiO_4 polymorphs. Phys Chem Miner 15: 181–190

Revenaugh J, Jordan TH (1991) Mantle layering from ScS reverberations. 2. The transition zone. J Geophys Res 96: 19763–19780.

Reynard B, Fiquet G, Itie JP, Rubie DC (1996) High-pressure X-ray diffraction study and equation of state of $MgSiO_3$ ilmenite. Am Mineral 81: 45–50

Rigden SM, Fitz Gerald JD, Jackson I, Gwanmesia GD, Liebermann RC (1991) Spinel elasticity and seismic structure of the transition zone of the mantle. Nature 354: 143–145

Ringwood AE (1975) Composition and Petrology of the Earth's Mantle, McGraw-Hill, New York

Ringwood AE (1979) Composition and origin of the Earth. In the Earth, its Origin, Structure and Evolution, McElhinny MW eds, Academic Press, New York, 1-58

Ringwood AE, Major A (1966) Synthesis of Mg_2SiO_4-Fe_2SiO_4 spinel solid solutions. Earth Planet Sci Lett 1: 241-245

Ringwood AE, Major A (1970) The system Mg_2SiO_4–Fe_2SiO_4 at high pressures and temperatures. Phys Earth Planet Inter 3: 89–108.

Ross NL, Hazen RM (1989) Single crystal X-ray diffraction study of $MgSiO_3$ perovskite from 77 to 400 K. Phys Chem Miner 16: 415–420

Ryberg T, Wenzel F, Egorkin AV, Solodilov L (1997) Short-period observation of the 520 km discontinuity in northern Eurasia. J Geophys Res 102: 5413–5422

Saikia A, Frost DJ, Rubie DC (2008) Splitting of the 520-kilometer seismic discontinuity and chemical heterogeneity in the mantle. Science 319: 1515–1518.

Sangster MJL, Peckham G, Saunderson DH (1970) Lattice dynamics of magnesium oxide. J Phys C: Solid State Phys 3: 1026–1036

Sawamoto H (1987) Phase diagram of $MgSiO_3$ at pressures up to 24 GPa and temperatues up to 2200◦C: Phase stability and properties of tetragonal garnet. In High Pressure Research in Mineral Physics, Manghnani M, Syono Y, eds. Geophysical Monograph 39, American Geophysical Union, 209–219

Shaner JW, Brown JM, McQueen RG (1984) In High Pressure in Science and Technology, Homan C, MacCrone RK, Whalley E, eds. Amsterdam: North-Holland, 137

Shearer PM (1990) Seismic imaging of upper-mantle structure with new evidence for a 520-km discontinuity. Nature 344 :121–126.

Shearer PM, Flanagan MP (1999) Seismic Velocity and Density Jumps Across the 410- and 660-Kilometer Discontinuities. Science 285: 1545–1548

Shen and Heinz D (1998) High pressure melting of deep mantle and core materials, Rev. Mineral Geochem 27: 369-396

Shim SN, Duffy TS, Shen G (2001) The post-spinel transformation in Mg_2SiO_4 and its relation to the 660-km seismic discontinuity. Nature 411: 571–574

Shim SN, Jeanloz R, and Duffy TS (2002) The tragonal structure of $CaSiO_3$ perovskite above 20 GPa, Geophys Res Lett 29: 2166-2169.

Shinmei T, Tomioka N, Fujino K, Kuroda K, Irifune T (1999) In situ X-ray diffraction study of enstatite up to 12 GPa and 1473 K and equations of state. Am Mineral 84: 1588–1594

Sidorin I, Gurnis M, Helmberger DV (1999) Evidence for a Ubiquitous Seismic Discontinuity at the Base of the Mantle. Science 286: 1326–1331

Sinogeikin SV, Bass JD, Katsura T (2003) Single-crystal elasticity of ringwoodite to high pressures and high temperatures: implications for 520 km seismic discontinuity. Phys Earth Planet Inter 136: 41–66

Smyth JR, Jacobsen, SD, Downs R T (2001) Comparative Crystal Chemistry of Orthosilicate Minerals. In High-temperature and high pressure crystal chemistry, Reviews in Mineralogy and Geochemistry, Hazen RM, Downs RT, eds., vol. 41, chap. 7. 187–209

Smyth JR, Kawamoto T, Jacobsen SD, Swope RJ, Hervig RL, Holloway JR (1997) Crystal structure of monoclinic hydrous wadsleyite [β-$(Mg, Fe)_2SiO_4$]. Am Mineral 82: 270–275

Speziale S, Zha C, Duffy TS, Hemley RJ, Mao HK (2001) Quasi-hydrostatic compression of magnesium oxide to 52 GPa: Implications for the pressure-volume-temperature equation of state. J Geophys Res 106: 515–528

Stackhouse S Brodholt J (2007) High temperature elasticity of $MgSiO_3$ post-perovskite, ed by Hirose K, Brodholt J, Lay T, Yuen D, Post-perovskite, The last mantle phase transition, AGU Monograph Series 174: 99-114.

Stixrude L (1997) Structure and sharpness of phase transitions and mantle discontinuities. J Geophys Res 102: 14835–14852

Stixrude L, Cohen RE, Yu R, Krakauer H (1996) Prediction of phase transition in $CaSiO_3$ perovskite and implications for lower mantle structure, Am Mineral 81:1293-1296

Stixrude L, Lithgow-Bertelloni C (2005) Mineralogy and elasticity of the oceanic upper mantle: Origin of the low-velocity zone. J Geophys Res 110: B3204

Stixrude L, Lithgow-Bertelloni C, Kiefer B, and Fumagalli P (2007) Phase stability and shear softening in $CaSiO_3$ perovskite at high pressure, Phys Rev B 75: 024108

Strachan A, Cagin T, Goddard WA (1999) Phase diagram of MgO from density-functional theory and molecular-dynamics simulations. Phys Rev B 60: 15084–15093

Suito K (1977) Phase relations of pure Mg_2SiO_4 up to 200 kilobars. In High Prssure Research—Applications to Geophysics, Manghnani MH, Akimoto S, eds. Academic Press, New York, 255–266

Suzuki A, Ohtani E, Morishima H, Kubo T, Kanbe Y, Kondo T, Okada T, Terasaki H, Kato T, Kikegawa T (2000) In situ determination of the phase boundary between wadsleyite and ringwoodite in Mg_2SiO_4. Geophys Res Lett 27: 803–806

Suzuki I, Ohtani E, Kumazawa M (1979) Thermal expansion of γ-Mg_2SiO_4. J Phys Earth 27: 53–61

Suzuki I, Ohtani E, Kumazawa M (1980) Thermal expansion of modified spinel, β-Mg_2SiO_4. J Phys Earth 28: 273–280

Suzuki I, Takei H, Anderson OL (1984) Thermal expansion of single-crystal forsterite Mg_2SiO_4. In the proceedings of the eighth international thermal expansion symposium, 79–88

Troullier N, Martins JL (1991) Efficient pseudopotentials for plane-wave calculations. Phys Rev B 43: 1993

Tsuchiya T (2003) First-principles prediction of the P-V-T equation of state of gold and the 660-km discontinuity in Earth's mantle. J Geophys Res 108: 2462

Tsuchiya J, Tsuchiya T, Wentzcovitch RM (2005) Vibrational and thermodynamic properties of $MgSiO_3$ postperovskite. J Geophys Res 110: 2204

Tsuchiya T, Tsuchiya J, Umemoto K,Wentzcovitch RM (2004) Phase transition in $MgSiO_3$ perovskite in the earth's lower mantle. Earth Planet Sci Lett 224: 241–248

Vanderbilt D (1990) Soft self-consistent pseudopotentials in a generalized eigenvalue formalism. Phys Rev B 41: 7892–7895

Vočadlo L, Alfè D (2002) Ab initio melting curve of the fcc phase of aluminum. Phys Rev B 65: 214105

Umemoto K, Wentzcovitch RM, Allen PB (2006) Dissociation of $MgSiO_3$ in the cores of giants and terrestrial exoplanets, Science 311: 983-986.

Wang YB, Weidner DJ (1994) Thermoelasticity of $CaSiO_3$ perovskite and implications for the lower mantle. Geophys Res Lett 21: 895-898

Wang Y, Weidner DJ, Liebermann RC, Zhao Y (1994) P-V-T equation of state of $(Mg,Fe)SiO_3$ perovskite: constraints on composition of the lower mantle. Phys Earth Planet Inter 83: 13–40

Wallace DC (1972) thermodynamics of crystal. Wiley, New York

Watanabe H (1982) Thermochemical properties of synthetic high pressure compounds relevant to the earth's mantle. In High pressure research in Geophysics, Akimoto S, Manghnani M, eds. Center for Academic Publishing of Japan, 441–464

Weidner D, Sawamoto H, Sasaki S, Kumazawa M(1984) Single-crystal elastic properties of the spinel phase of Mg_2SiO_4. J Geophys Res 89: 7852–7860

Weidner DJ, Wang Y (2000) Phase transformations: Implications for mantle structure. In Earth's deep interior: mineral physics and tomography from the atomic to the global scale. Geophys Monogr 117: 215-235

Wentzcovitch RM (1991) Invariant molecular-dynamics approach to structural phase transitions. Phys Rev B 44: 2358–2361

Wentzcovitch RM, Martins JL, Price GD (1993) Ab initio molecular dynamics with variable cell shape: application to MgSiO3. Phys Rev Lett 70: 3947

Wentzcovitch RM, Hugh-Jones DA, Angel RJ, Price GD (1995) Ab initio study of $MgSiO_3$ C2/c enstatite. Phys Chem Mineral 22: 453-460

Wentzcovitch RM, Stixrude L (1997) Crystal chemistry of forsterite: a first-principles study. Am Mineral 82: 663– 671

Wentzcovitch RM, Stixrude L, Karki B, Kiefer B (2004) Akimotoite to perovskite Geohys Res Lett 31: L10611

Wentzcovitch RM, Karki BB, Cococcioni M, de Gironcoli S (2004) Thermoelastic Properties of $MgSiO_3$-Perovskite: Insights on the Nature of the Earth's Lower Mantle. Phys Rev Lett 92: 018501

Wentzcovitch RM, Tsuchiya T, Tsuchiya J (2006) $MgSiO_{3-}$ –post perovskite at D″ conditions, Proc Natl Acad Sc USA 103: 543-546 (2006)

Wentzcovitch RM, Umemoto K, Tsuchiya T, Tsuchiya J (2007) Thermodynamic properties and stability field of $MgSiO_3$ post-perovskite, ed by Hirose K, Brodholt J, Lay T, Yuen D, Post-perovskite, The last mantle phase transition, AGU Monograph Series 174: 79-98

Wiggins RA, Helmberger DV (1973) Upper mantle structure of the western United States. J Geophys Res 78: 1870–1880

Williams Q, Jeanloz R, McMillan P (1987) Vibrational spectrum of $MgSiO_3$ perovskite: Zero pressure raman and mid-infrared spectra to 27 GPa. J Geophys Res 92: 8116–8128

Wu Z, Wentzcovitch RM (2007) Vibrational and thermodynamic properties of wadsleyite: A density functional study. J Geophys Res 112: B12202

Wu Z, Wentzcovitch RM, Umemoto K, Li B, Hirose K, Zheng J-C (2008) Pressure-volume-temperature relations in MgO: An ultrahigh pressure-temperature scale for planetary sciences applications. J Geophys Res 113: B06204

Wu Z, Wentzcovitch RM (2009) Effective semiempirical ansatz for computing anharmonic free energies. Phys. Rev. B 79:104304

Yang H, Prewitt CT (2001) Chain and layer silicates at high temperatures and pressures. In High-temperature and high pressure crystal chemistry, Reviews in Mineralogy and Geochemistry, Hazen RM, Downs RT, eds, vol. 41. chap. 8. 211–255

Yu YG, Wentzcovitch RM (2006) Density functional study of vibrational and thermodynamic properties of ringwoodite. J Geophys Res 111: B12202

Yu YG, Wentzcovitch RM, Tsuchiya T, Umemoto K, Weidner DJ (2007) First principles investigation of the postspinel transition in Mg_2SiO_4. Geophys Res Lett 34: 10306

Yu YG, Wu Z, Wentzcovitch RM (2008) α-β-γtransformations in Mg_2SiO_4 in Earth transition zone. Earth Planet Sci Lett 34: 10306

Yu YG, Wentzcovitch RM (2008) Low pressure clino- to high pressure clinoenstatite phase transition: a phonon related mechanism, Am Mineral 94: 461-466.

Yu YG, Wentzcovitch RM, Angel RJ (2009) Thermodynamics properties of and phase boundary between low pressure and high pressure clinoenstatite, J Geophys Res, in press.

Yu YG, Angel RJ, Wentzcovitch RM (20010) Thermodynamics properties of $MgSiO_3$ majorite, in preparation.

Zerr A, Boehler R (1993) Melting of $(Mg,Fe)SiO_3$-Perovskite to 625 Kilobars: Indication of a High Melting Temperature in the Lower Mantle. Science 262: 553–555

Zerr A, Boehler R (1994) Constraints on the melting temperature of the lower mantle from highpressure experiments on MgO and magnesiowüstite. Nature 371: 506–508

Zerr A, Diegeler A, Boehler R (1998) Solidus of Earth's Deep Mantle. Science 281: 243–246

Zerr A, Serghiou G, Boehler R (1997) Melting of $CaSiO_3$ perovskite to 430 kbar and first in-situ measurements of lower mantle eutectic temperatures. Geophys. Res. Lett. 24, 909-912

Zouboulis ES, Grimsditch M (1991) Raman scattering in diamond up to 1900 K. Phys Rev B 43: 12490-12493

Table 1 - Comparison between measured thermodynamic properties of various magnesium silicates and quasiharmonic LDA and GGA (PBE) results at 300 K and room pressure (3rd order Birch-Murnaghan equation of state was used in this calculation).

	V (A^3/uc)	**K_T (GPa)**	**K_T'**	**α (10^{-5} K^{-1})**	**Cp (J/mol/K)**	**γ**
			MgO			
exp	74.8	160(2)	4.15	3.12(16)	37.67	1.54(8)
LDA	75.2	161.7	4.1	3.15	37.62	1.61
GGA	77.5	155.7	3.8	3.22	38.6	1.54
			Forsterite			
exp	289.2 | 291.9	125 | 127.7	4.0	2.48 | 2.83	117.9	1.28
LDA	290.3	127.4	4.3	2.66	119.5	1.25
GGA	302.0	112.2	4.3	3.19	122.8	1.31
			Wadesleyite			
exp	535.3 | 539.3	160(3) | 172(3)	4.3 | 4.8	2.06	114.14	1.26
LDA	541.34	165.7	4.4	2.21	118.1	1.28
GGA	559.2	156.5	3.8	2.47	121.1	1.35
			Ringwoodite			
exp	526.7(3)	183(3)	4.2(3)	1.8 | 2.5	113.0	1.25
LDA	527.5	184.7	4.3	1.97	116.9	1.22
GGA	544.4	169.3	4.2	2.24	120.2	1.33
			Perovskite			
exp	162.5	246 | 272	3.9 | 4.0	1.7 | 2.2	80.6	1.3 | 1.96
LDA*	164.2	243.1	4.1	2.19	82.81	1.61
GGA*	169.7	223.7	3.9	2.46	85.9	1.72
			Post-perovskite			
exp$	81.15 | 81.9	222 | 259.5	3.69 | 4.4	1.70#	---	---
LDA	81.8	223.1	4.2	2.35	82.2	1.65
GGA	85.0	196.2	4.2	2.76	85.5	1.62
			Stishovite			
exp	46.51	309.9	4.59	1.46	42.48	---
LDA	47.0	294.4	4.6	1.18	42.1	1.2
GGA	48.6	267.3	4.3	1.40	43.8	1.25
			LP-Clinoenstatite			
exp	415.4(5),	108.5(6.3),	4.5(1.3)	---	---	---

	414.6(1)	111.1(3.3)				
LDA	415.2	121.5	5.5	2.5	81.67	1.16
GGA	433.7	102.0	5.5	3.2	83.8	1.27
			HP-Clinoenstatite			
exp	405.1(1.7)	106.4(17.4), 106.9(25.9)	5.4(2.7), 5.3(3.0)	2.64	81.95	---
LDA	397.1	126	5.5	2.46	81.09	1.16
GGA	423.3	94.4	6.4	3.4	83.9	1.12
			Ilmenite			
exp	43.76	212	7.5(1.0), 5.6(1.0)	1.67	78.0	---
LDA	44.2	201.7	4.4	1.92	80.1	1.3
GGA	45.3	207.5	3.7	1.95	81.8	1.35
			Majorite			
exp	759.3	159.8(4.4)	5.8	---	---	---
LDA	759.6	160.7	4.3	2.4	82.8	1.3
GGA	792.2	137.8	4.3	2.9	85.2	1.41

Experimental data are separated by semicolons in each phase from other calculation sources, for most of which the detailed calculated values are not shown here because of inequivalence posed by using different pseudopotentials and other convergence parameters.

MgO: Fei (1999), Isaak et al. (1989), Touloukian et al. (1977); Karki et al. (1999)
Forsterite: Guyot et al. (1996), Downs et al. (1996), Gillet et al. (1991), Bouhifd et al. (1996); Li et al (2007), Yu et al (2008), Price et al. (1987), da Silva et al. (1997), Wentzcovitch and Stixrude (1997)
Wadsleyite: Hazen et al. (1990), Hazen et al. (2000), Horiuchi and Sawamoto (2000), Suzuki et al. (1980), Ashida et al. (1987); Wu and Wentzcovitch (2007)
Ringwoodite: Meng et al. (1994), Chopelas et al. (1994), Li (2003), Jackson et al. (2000), Weidner et al. (1984), Katsura et al. (2004b) Suzuki et al. (1979), Chopelas (2000); Yu et al. (2006), Kiefer et al. (1997), Piekarz et al. (2002)
Perovskite: Knittle et al. (1986), Mao et al. (1991), Ross and Hazen (1989), Wang et al. (1994), Chopelas (1999); [*]Tsuchiya et al. (2005), Karki et al. (2000b), Wentzcovitch et al. (1995)
[$]**Post-perovskite**: both experiments and calculations are incooperated. Murakami et al. (2004), Komabayashi et al. (2008)[#], [#] thermal expansion value of pv was assumed to be that of ppv at ambient condition; Tsuchiya et al. (2004), Oganov and Ono (2004)
Stishovite: Akaogi et al. (1995), Andrault et al. (2003); Oganov et al. (2005), Umemoto et al. (2006)
LP-Clinoenstatite & HP- Clinoenstatite: Angel and Hugh-Jones (1994), Shinmei et al. (1999); Yu et al (2009), Wentzcovitch (1995), Duan et al. (2001)
Ilmenite: Horiuchi et al. (1982), Reynard et al. (1996), Chopelas (1999); Karki and Wentzcovitch (2002)
Majorite: Angel et al. (1989), Gerald Pacalo and Weidner (1997); Downs and Bukowinski (1997), Yu et al to be published(2010)

Table 2 - Comparison of LDA and GGA Clapeyron slopes from this study with those determined by experiments and other calculations.

Series	**transition**	**GGA**	**LDA**	**Exp. and others calc.**						
				1	2	3	4	5	6	7
A	α to β	2.7	2.5	3.5	4.1±0.7	2.5	1.8	2.7	3.6	4.0
B	β to γ	3.6	3.5	4.4	4.2	6.9	4.1	6.3	4.5	
C	γ to pc+pv	-2.8	-2.7	-2.8	-2.5	-2.75	-2 | -0.4	-1.3	-0.5	
D	LP-En to HP-En	3.0	2.9	2.0	1.6					
E	pv to ppv	---	---	7.5 ±0.3	9.6 | 9.9	5.0 | 11.5	6	9.7	7.0	

Experimental data and other calculation sources:
α to β --- LDA and GGA: Yu et al. 2008, [A1]: Suito 1977, [A2] Watanabe 1982, [A3]: Katsura and Ito 1989, [A4]: Akaogi et al. 1989, [A5]: Price et al. 1987, Chopelas 1991, [A6]: Morishima et al. 1994, Stixrude and Lithgow-Bertelloni 2005, [A7]: Katsura et al. 2004a
β to γ --- LDA and GGA: Yu et al. 2008, [B1]: [A3], [B2]: [A4], [B3]: Suzuki et al. 2000, [B4]: Inoue et al. 2006, [B5]: Sawamoto 1987, [B6]: Price et al. 1987
γ to pc+pv --- LDA and GGA: Yu et al. 2008, [C1]: Ito and Takahashi 1989, [C2]: Irifune et al. 1998, [C3]: Shim et al. 2001, [C4]: Katsura et al. 2003, [C5]: Fei et al. 2004, [C6]: Litasov et al. 2005
LP-En to HP-En --- Yu et al. 2008, [D1]: Gasparik 1990, [D2]: Angel and Hugh-Jones 1994
pv to ppv --- [E1]: Tsuchiya et al. 2004, [E2]: Oganov and Ono 2004, [E3]: Hirose 2006 and references therein, [E4]: Sidorin et al. 1999, [E5] Wu et al. 2008, [E6] Ono and Oganov 2005

Table 3 - Calculated (LDA) properties of Mg_2SiO_4 along the (GGA) phase boundary for *α–β* transition (~1500 K, 16.3 GPa)) (Yu et al. 2008), *β–γ* transition (~1700 K, 20.2 GPa) (Yu et al. 2008), and γ-dissociation transition (1900 K and 23.2 GPa) (Yu et al. 2007) compared with seismic data on the 410-, 520-, and 660-km discontinuities and mineral physics experiments.

	ρ			K_S			V_Φ		
transition	calc.	PREM	oth.	calc.	PREM	oth.	calc.	PREM	oth.
				410-km					
Upper 410 (α)	3.47	3.54	---	178.3	173.5	---	7.17	7.00	---
Lower 410 (β)	3.65	3.72	---	218.3	189.9	---	7.73	7.14	---
%Δ 410 (α→β)	5.1%	5.0%	~0.2–4%[a]	20.2%	9.0%	---	7.6%	1.9%	1.5–6.6%[a]
				520-km					
Upper 520 (β)	3.70	3.85[§]	---	231.9	218.1[§]	---	7.91	7.54[§]	---
Lower 520 (γ)	3.77	---	---	249.5	---	---	8.13	---	---
%Δ 520 (β→γ)	1.8%	---	1.3–2.9%[b], 2.5–3.0%[c], 2.5%[d]	7.3%	---	---	2.7%	---	1.3–2.1%[b]
				660-km					
Upper 660 (γ)	3.81	3.99	---	261.1	255.8	---	8.274	8.007	---
Lower 660 (pv + pc)	4.13	4.38	---	282.1 ± 2.8*	299.4	---	8.266 ±0.080*	8.268	---
%Δ 660 (γ→ pv + pc)	7.9%	9.3%	5.2%[a]	7.7 ±1.0%*	15.9%	5.5%[a]	-0.10 ±0.48%*	3.2%	0.16%[a]

* uncertainties from VRH average of pv+pc aggregate, [§]PREM at 500-km,
[a] Shearer and Flanagan(1999), [b] Lawrence and Shearer (2006), [c] Rigden et al. (1991),
[d] Sinogeikin et al. (2003).

Table 4 - Thermodynamic properties of the investigated phases at relevant mantle conditions, before and after inclusion of anharmonic effects (from Wu and Wentzcovitch, 2009).

MgO at 2000K and 23 GPa				
c	α (10^{-5}/K)	γ	C_p (J mol^{-1} K^{-1})	K_S (GPa)
0	3.25	1.437	54.07	224.917
0.1	3.04	1.38	52.79	226.822
Change (%)	-6.5	-4.0	-2.4	0.8
MgO at 4000K and 135 GPa				
c	α (10^{-5}/K)	γ	C_p (J/ mol K)	K_S (GPa)
0	1.31	1.202	52.769	598.19
0.1	1.268	1.178	52.025	597.64
Change (%)	-3.2	-2.2	-1.4	-0.09
Forsterite at 1700 K and 13.5GPa				
c	α (10^{-5}/K)	γ	C_p (J/mol K)	K_S (GPa)
0	2.862	1.078	180.549	164.267
-0.06	2.96	1.102	182.008	163.763
Change (%)	3.5	2.2	0.8	-0.3
Wadsleyite at 1700K and 13.5GPa				
c	α (10^{-5}/K)	γ	C_p (J/molK)	K_S (GPa)
0	2.674	1.173	180.77	202.105
0.08	2.564	1.141	178.85	203.01693
Change (%)	-4.1	-2.7	-1.0	0.45

Table 5 - Measured and calculated Clapeyron slopes (MPa/K) of the thermodynamic boundary between forsterite (α) and wadsleyite (β) (from Wu and Wentzcovitch 2009).

High pressure experiments	2.5	Katsura and Ito, 1989
	3.5	Suito, 1977
	3.6	Morishma et al., 1994
	4.0	Katsura et al., 2003
QHA based calculations	1.8	Akaogi et al.1989
	2.7	Price et al.,1987; Chopelas, 1991; Yu et al., 2008
This study	3.6	using c = -0.06 for α-phase and c = 0.08 for β-phase

Figure Captions

Figure 1 - (a) Velocities and density profiles (Kennett et al. 1995), (b) Earth's cross section, and (c) composition and mineralogy of Earth's layers.

Figure 2 - Phases proportions versus depth and or pressure. **Ol** = $(Mg,Fe)_2SiO_4$ olivine, also known as α-phase; **β** =$(Mg,Fe)_2SiO_4$ wadsleyite, also known as β-phase; **γ** = $(Mg,Fe)_2SiO_4$ ringwoodite, also known as γ-phase; **Gt** = garnet; **Mj-Gt** = majorite garnet, solid solution between pyrope $Mg_3Al_2(SiO_4)_3$ and majorite $MgSiO_3$ joint, **CPx** = clinopyroxene; **OPx** = orthopyroxene; **Ca-Pv** = CaSiO3-perovskite; **(Mg,Fe,Al)-perovskite** = $(Mg,Al,Fe)(Si,Al)O_3$; **post-perovskite** = $(Mg,Al,Fe)(Si,Al)O_3$ **ferropericlase** = (Mg,Fe)O.

Figure 3 - Illustration of melting temperature of mantle minerals (from Zerr, Diegler, Boehler, 1998). HA is the shock melting point of olivine (Holland and Ahrens, 1997). For a more complete overview of experimental melting temperatures of mantle minerals, see Shen and Heinz (1998). Mantle temperature is according to Brown and Shankland (1981). The considerable difference between melting temperatures and expected mantle temperatures, suggested the use of the quasiharmonic approximation (QHA) to investigate thermodynamics properties of minerals at mantle conditions. [Used by permission of Science, from Zerr et al. 1998].

Figure 4 -Phonon dispersion of MgO at 0 and 100 GPa (from Karki et al. 2000). Inelastic neutron scattering data by Sangster et al. 1970 in circles (0 GPa). [Used by permission of APS, from Karki et al. 2000a].

Figure 5 - Helmholtz free energy vs. volume of MgO at various temperatures (Karki et al., 1999). Static means 0 K without lattice zero point motion effects.

Figure 6 - Crystal structures of (left) $MgSiO_3$-perovskite (*Pbnm*) and (right) post-perovskite (*Cmcm*). In post-perovskite, top, bottom left and bottom right views are along [010], [100], and [001] respectively.

Figure 7 - Left: LDA phonon dispersions and density of states of $MgSiO_3$ perovskite along a few high symmetry lines in the first Brillouin zone (Karki et al., 2000). Right: comparison with experimental Raman and infrared spectroscopy at 0 GPa. Experimental data from Williams et al. (1987), D.J. Durben and G.H. Wolf (1992); Lu et al. (1994); Chopelas (1996); Lu and Hofmeister (1994). [Used by permission of APS, from Karki et al. 2000b].

Figure 8 - Thermal expansivity, $\alpha(P,T)$, of $MgSiO_3$-perovskite (from Carrier et al., 2007). The black line, labeled "QHA boundary," is defined by the position of the inflection points of $\alpha(P,T)$, as described in the text. [Used by permission of APS, from Carrier et al. 2007].

Figure 9 - The valid (*P,T*) region of QHA (Tsuchiya et al., 2005). The solid and dashed lines show the valid range of the QHA for calculations in postperovskite and perovskite, respectively. Thick dashed line indicates the Brown and Shankland (1981) mantle geotherm. [Used by permission of AGU, from Tsuchiya et al. 2005].

Figure 10 - Comparison between the limit of QHA validity with melting temperatures for aluminum and periclase. The QHA validity limit was determined according to the criterion based on the inflection point in the thermal expansivity. Aluminum: (a) Boehler and Ross (1997); (b) Shaner et al. (1984); (c) Vocadlo and Alfe' (2002). MgO: (a) Zerr and Boehler (1994); Strachan et al. (1999).

Figure 11 - Crystal structures of SiO_2 stishovite (*$P4_2/mnm$*). Silicon sits in the center of oxygen octahedra.

Figure 12 - Crystal structures of forsterite (*Pbnm*), α-, wadsleyite (*Imma*), β-, and ringwoodite (*Fd-3m*), γ-Mg_2SiO_4. Oxygen and magnesium are shown in small and large spheres while silicon atoms sit in the centers of SiO_4 tetrahedra.

Figure 13 - Crystal structure of low pressure (*$P2_1/c$*) and high pressure (*C2/c*) $MgSiO_3$-clinoenstatite. The spheres represent magnesium in between the SiO_4 tetrahedral chains. [Used by permission of AMS, from Yu and Wentzcovitch 2008].

Figure 14 – (left) Crystal structure of $MgSiO_3$-ilmenite (*R-3*) and (right) tetragonal $MgSiO_3$-majorite (*$I4_1/a$*). Light and dark octahedral in ilmenite represent SiO_6 and MgO_6 units with spheres denoting oxygens. In tetragonal majorite, the 8-fold coordinated magnesium is shown as spheres. 6-fold coordinated ones are at the center of light octahedra. Silicon ions partition between SiO_4 (dark) tetrahedra and SiO_6 (light) octahedra.

Figure 15 - Predicted $CaSiO_3$ phase diagram showing the tetragonal to cubic phase boundary in LDA (thick line) and GGA (thin). Phase boundaries are dashed within the thermodynamic stability field of non-perovskite structures (Akaogi et al 2004). The orthorhombic to tetragonal transition is indicated by the nearly vertical dashed lines. Location of the transition to the cubic phase from molecular dynamics simulations are shown in yellow: dot-dashed (Adams and Oganov 2006) and dashed (Li et al 2006). Experimental data for the tetragonal and cubic phases are in blue and red (diamonds (Shim et al 2002), triangles (Ono et al 2004), circles (Kurashina et al 2004)). Squares are experimental results for a sample with 5 wt % Al_2O_3 (Kurashina et al 2004): green: orthorhombic, red: cubic. The red curve is the melting line (Zerr et al 1997). [Used by permission of APS, from Stixrude et al. 2007].

Figure 16 - Comparison between calculated and experimental phase boundaries for the α- to β- (top) and β- to γ-phase transitions (bottom) in Mg_2SiO_4 (from Yu et al. 2008). [Used by permission of EPSL, fromYu et al. 2008].

Figure 17 – Phase boundary of the post-spinel phase transition (dissociation of ringwoodite into $MgSiO_3$-perovskite and MgO) calculated by LDA and GGA compared to various experimental determinations (from Yu et al. 2007). [Used by permission of AGU, from Yu et al. 2007].

Figure 18 - Calculated changes in density, ρ, adiabatic bulk modulus, K_S, and bulk velocity, V_Φ, for phase transitions in Mg_2SiO_4 in the transition zone: the (a) α–β–γ transitions (from Yu et al. 2008) and the (b) γ dissociation (from Yu et al. 2007). See Yu et al. (2008) for an extensive discussion. [Used by permission of AGU and EPSL, fromYu et al. 2007, Yu et al. 2008].

Figure 19 - Density discontinuities in a mineral aggregate produced by the (a) α-to-β transition at 410-km versus volume fraction of α, compared to the best estimate from seismic data, 0.9% (Shearer and Flanagan 1999); (b) same for the β-to-γ transition at 520-km, compared with the estimated value of 2.1±0.8% (Lawrence and Shearer 2006), and (c) for the γ dissociation at 660-km, compared to the estimated value of 5.2% (Shearer and Flanagan 1999). Comparison is also made with PREM (Dziewonski and Anderson 1981). [Used by permission of AUG and EPSL, fromYu et al. 2007, Yu et al. 2008].

Figure 20 - Illustration of how a combination of DFT based calculations and experimental data can be used to constrain the triple point in the LP-En, HP-En, and orthorenstatite system (from Yu et al. 2009). [Used by permission of AGU, from Yu et al. 2009].

Figure 21 – Predicted phase boundary of the post-perovskite transition obtained by LDA and GGA (Tsuchiya et al., 2004). Star is from Murakami et al. (2004); dashed line corresponds to the Clapeyron slope predicted by Sidorin et al. (1999). For an extensive review of results see Hirose 2006. [Used by permission of EPSL, from Tsuchiya et al. 2004].

Figure 22 - Thermodynamic properties of MgO for several values of c (see Eq. (5.3)). c=0 corresponds to quasiharmonic results. (a) Thermal expansivity α, (b) thermal Grüneisen parameter, γ_{th}, (c) isobaric specific heat C_p, and (d) adiabatic bulk modulus (from Wu and Wentzcovitch, 2009). [Used by permission of APS, from Wu and Wentzcovitch 2009].

Figure 23 (a) Isobaric specific heat C_p at 0 GPa of forsterite (-phase) for several values of c. The inset shows the root–mean-square (RMS) of the difference between calculated and experimental C_p from Orr (1993) (dashed line), Anderson et al (1991) (dotted line), Gillet et al (1991) (dashed dotted line), and all data above (solid line). (b) Thermal expansivity, α, of wadsleyite for various values of c (from Wu and Wentzcovitch, 2009). [Used by permission of APS, from Wu and Wentzcovitch 2009].

Figure 24 - Phase boundary of the forsterite-to-wadsleyite (α-to-β) transformation predicted by LDA (left) and GGA (right) quasiharmonic calculations (dashed lines) and calculations including anharmonic contributions to the free energy according to Eqs. (9-

11) using c_α= -0.06 and c_β=0.08 (thick solid line). Other boundaries are from Katsura et al. (2003), Katsura and Ito (1989), Morishima et al. (1994) (M94), Suito (1977) (S77), Chopelas (1991) (C91) and Akaogi et al. (1989) (A89) (from Wu and Wentzcovitch, 2009). [Used by permission of APS, from Wu and Wentzcovitch 2009].

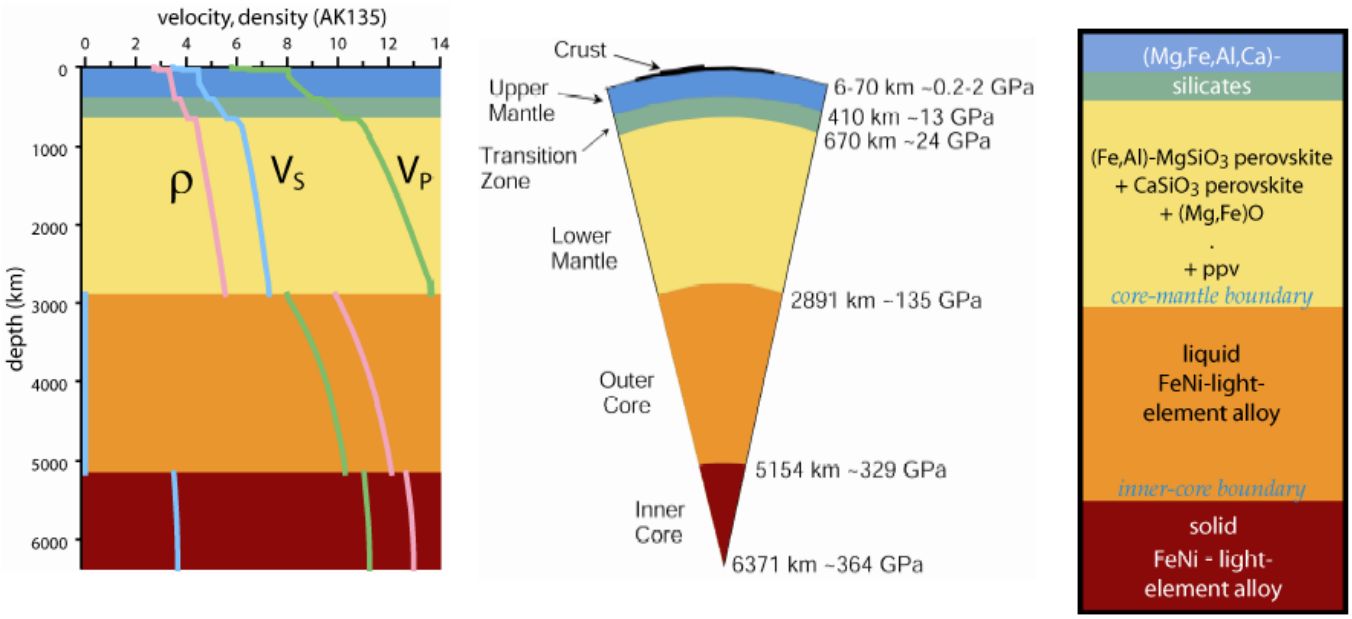
velocity, density (AK135)
0
2
4
6
8
10
12
14
depth (km)
0
1000
2000
3000
4000
5000
6000
ρ
V_S
V_P
Crust
Upper Mantle
Transition Zone
Lower Mantle
Outer Core
Inner Core
6-70 km ~0.2-2 GPa
410 km ~13 GPa
670 km ~24 GPa
2891 km ~135 GPa
5154 km ~329 GPa
6371 km ~364 GPa
(Mg,Fe,Al,Ca)-silicates
(Fe,Al)-MgSiO3 perovskite
+ CaSiO3 perovskite
+ (Mg,Fe)O
+ ppv
core-mantle boundary
liquid FeNi-light-element alloy
inner-core boundary
solid FeNi - light-element alloy

Figure 1

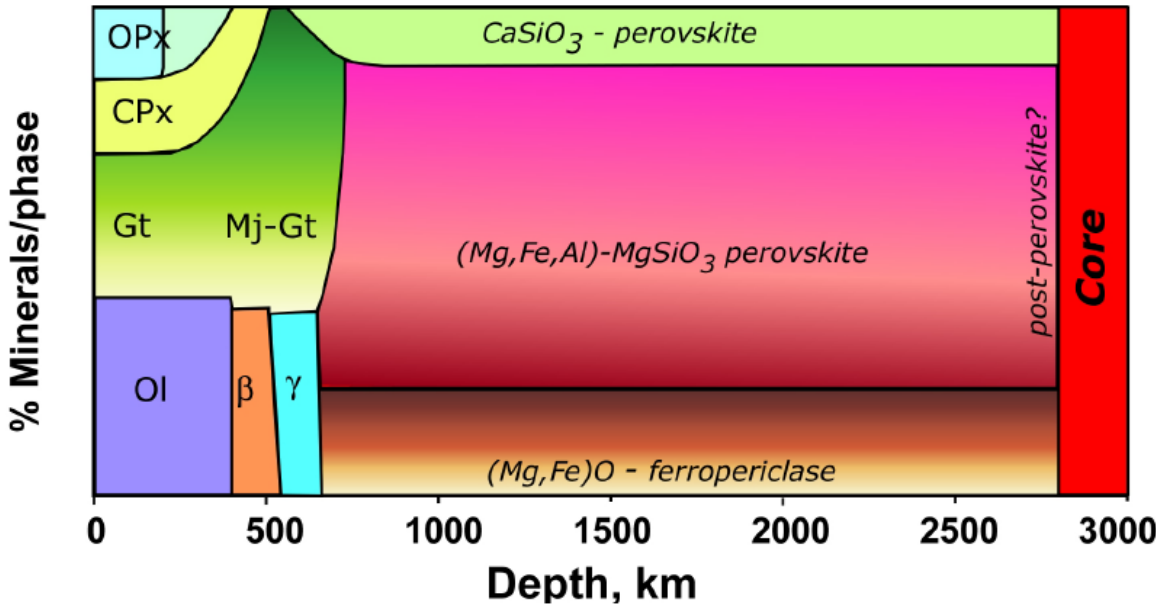
OPx
CPx
Gt
Mj-Gt
Ol
β
γ
CaSiO3 - perovskite
(Mg,Fe,Al)-MgSiO3 perovskite
post-perovskite?
Core
(Mg,Fe)O - ferropericlase
% Minerals/phase
0
500
1000
1500
2000
2500
3000
Depth, km

Figure 2

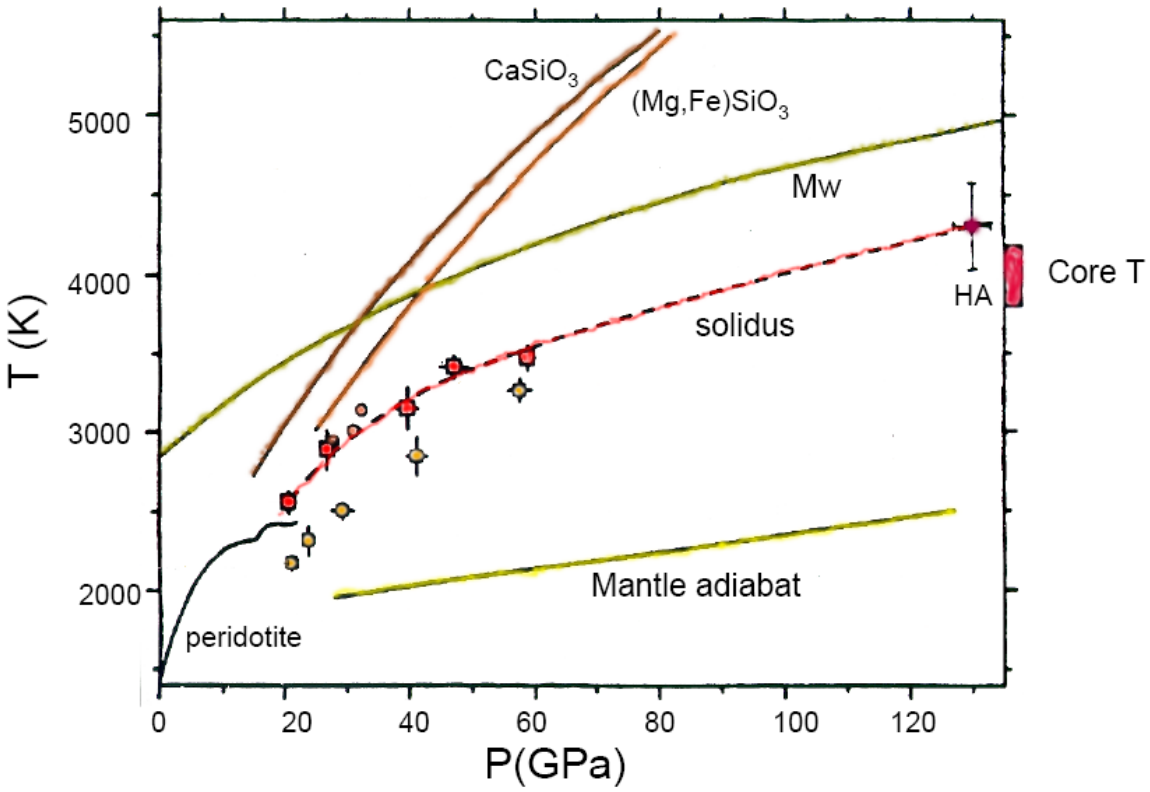
CaSiO3
(Mg,Fe)SiO3
Mw
solidus
HA
Core T
Mantle adiabat
peridotite
T (K)
P(GPa)
5000
4000
3000
2000
0
20
40
60
80
100
120

Figure 3.

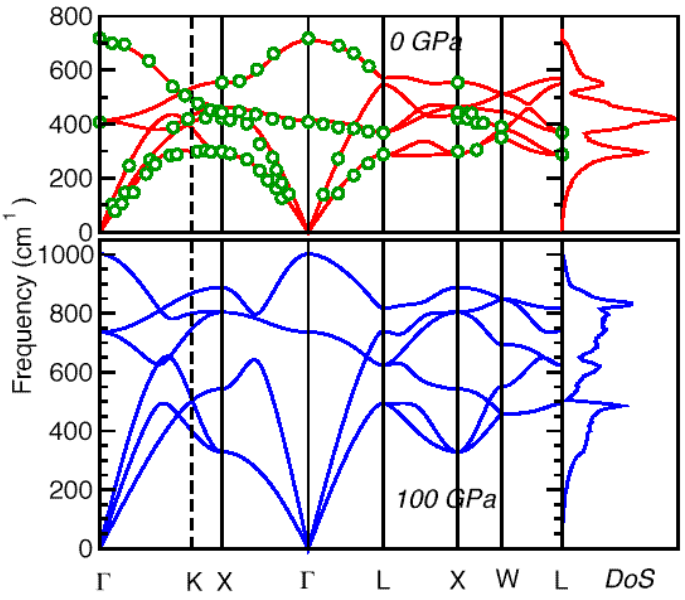
0 GPa
100 GPa
Frequency (cm^{-1})
800
600
400
200
0
1000
800
600
400
200
0
Γ
K
X
Γ
L
X
W
L
DoS

Figure 4

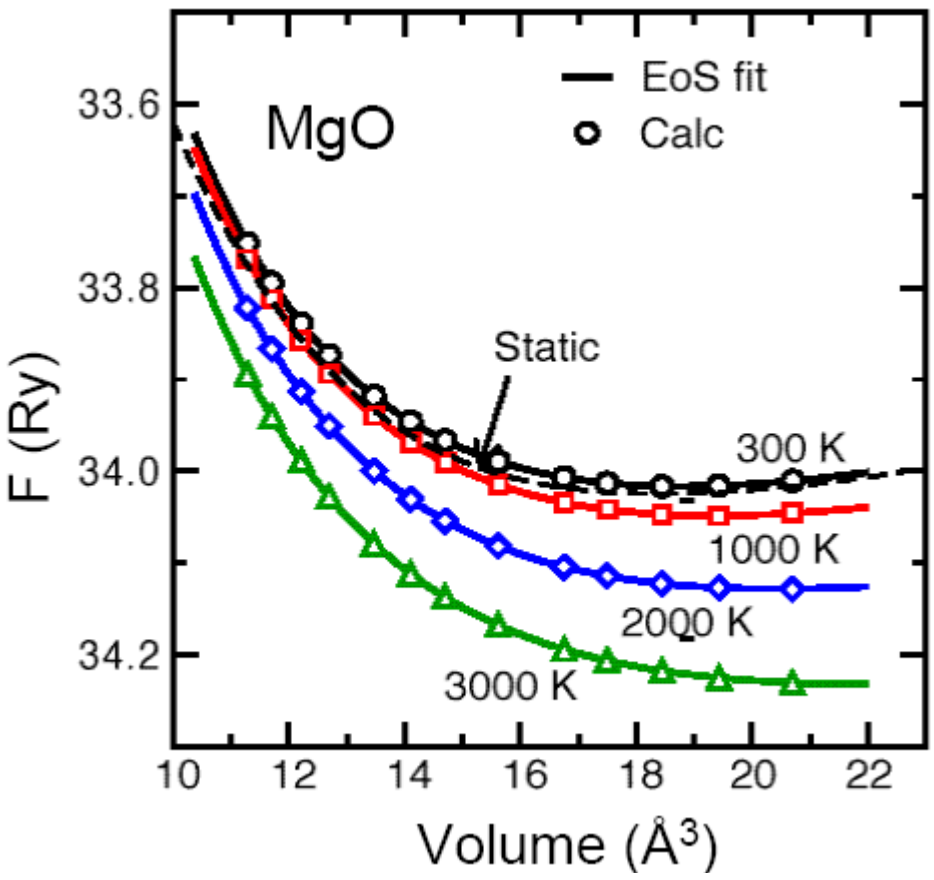
MgO
EoS fit
Calc
Static
300 K
1000 K
2000 K
3000 K
F (Ry)
33.6
33.8
34.0
34.2
10
12
14
16
18
20
22
Volume (Å3)

Figure 5.

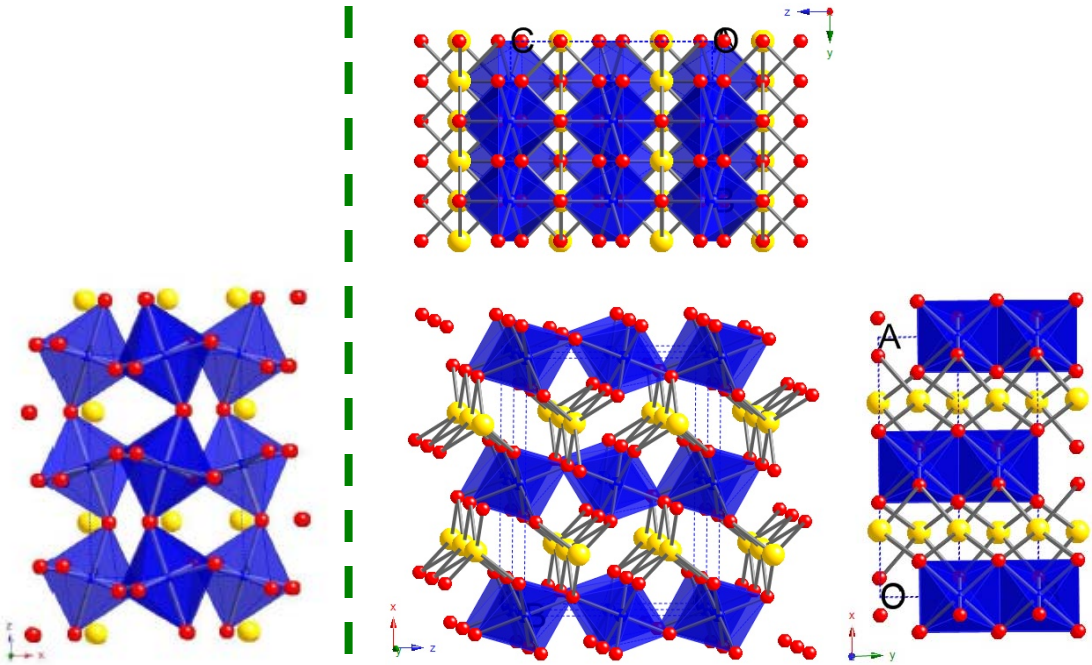

Figure 6 -

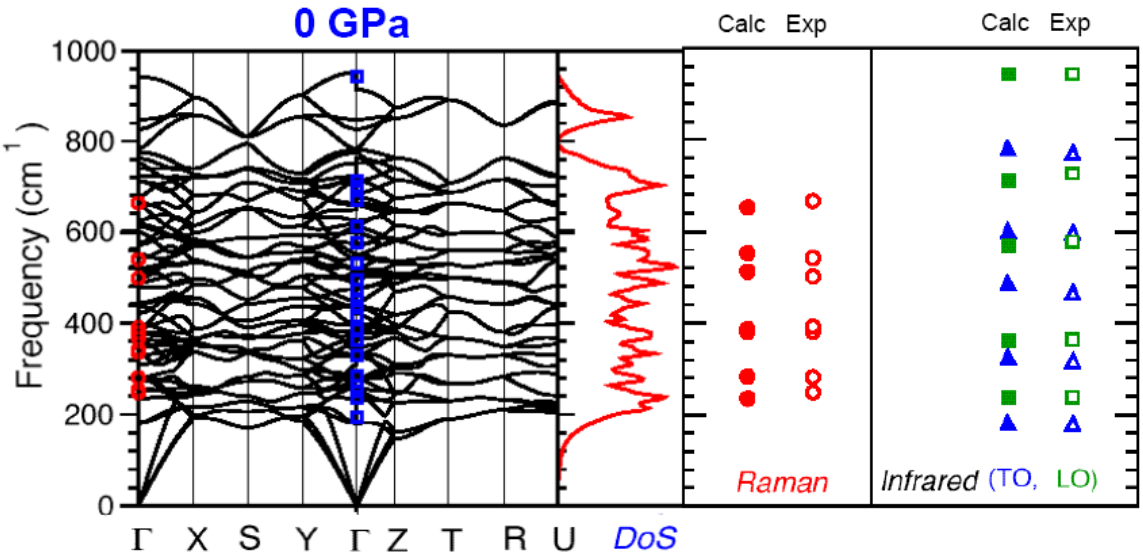
0 GPa
Calc Exp
Calc Exp
Frequency (cm-1)
1000
800
600
400
200
0
Γ X S Y Γ Z T R U
DoS
Raman
Infrared (TO, LO)

Figure 7

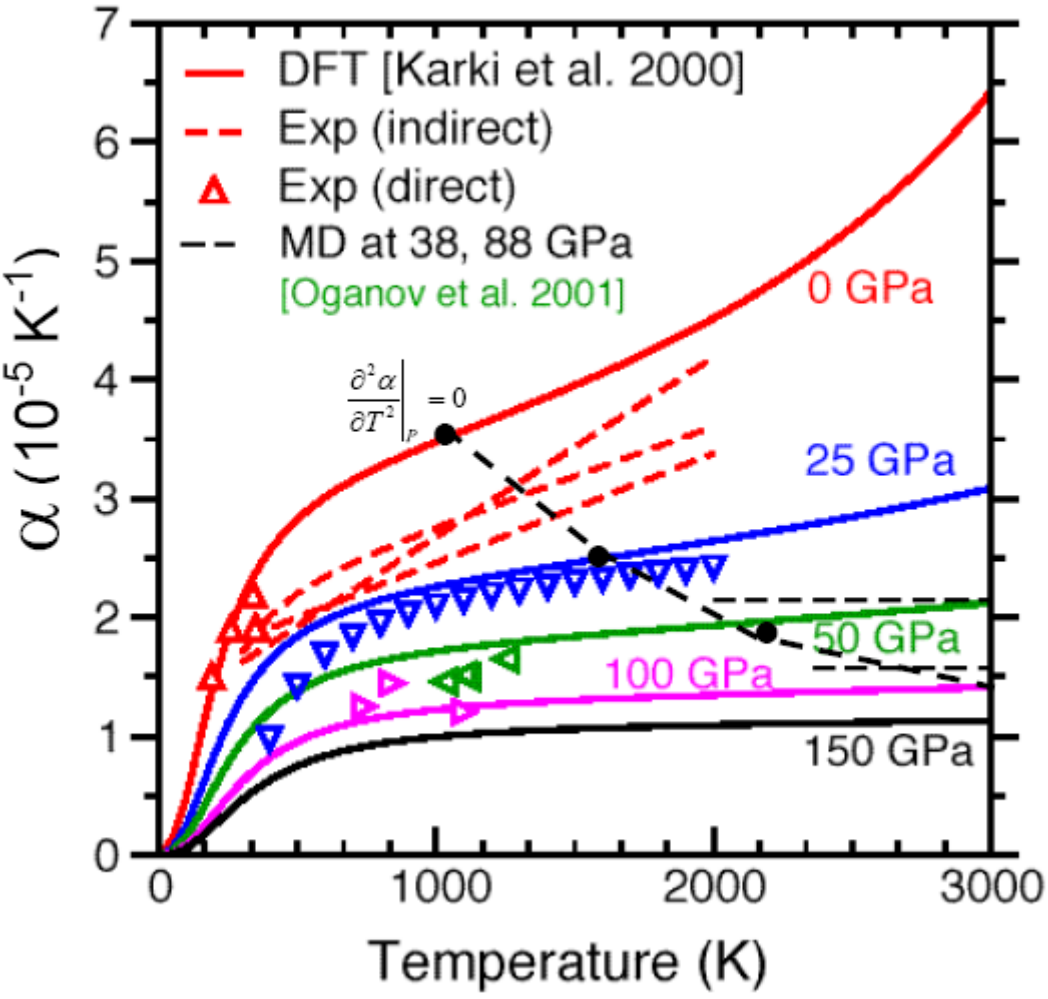
DFT [Karki et al. 2000]
Exp (indirect)
Exp (direct)
MD at 38, 88 GPa
[Oganov et al. 2001]
$\left.\frac{\partial^2 \alpha}{\partial T^2}\right|_P = 0$
0 GPa
25 GPa
50 GPa
100 GPa
150 GPa
α (10^-5 K^-1)
Temperature (K)
0
1000
2000
3000
1
2
3
4
5
6
7

Figure 8

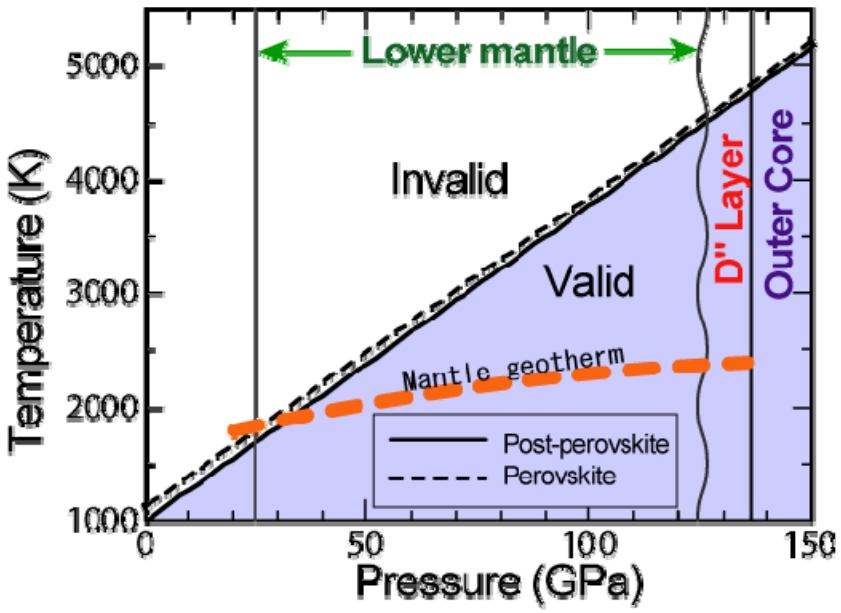
Lower mantle
Invalid
Valid
D'' Layer
Outer Core
Mantle geotherm
Post-perovskite
Perovskite
Temperature (K)
Pressure (GPa)
5000
4000
3000
2000
1000
0
50
100
150

Figure 9 -

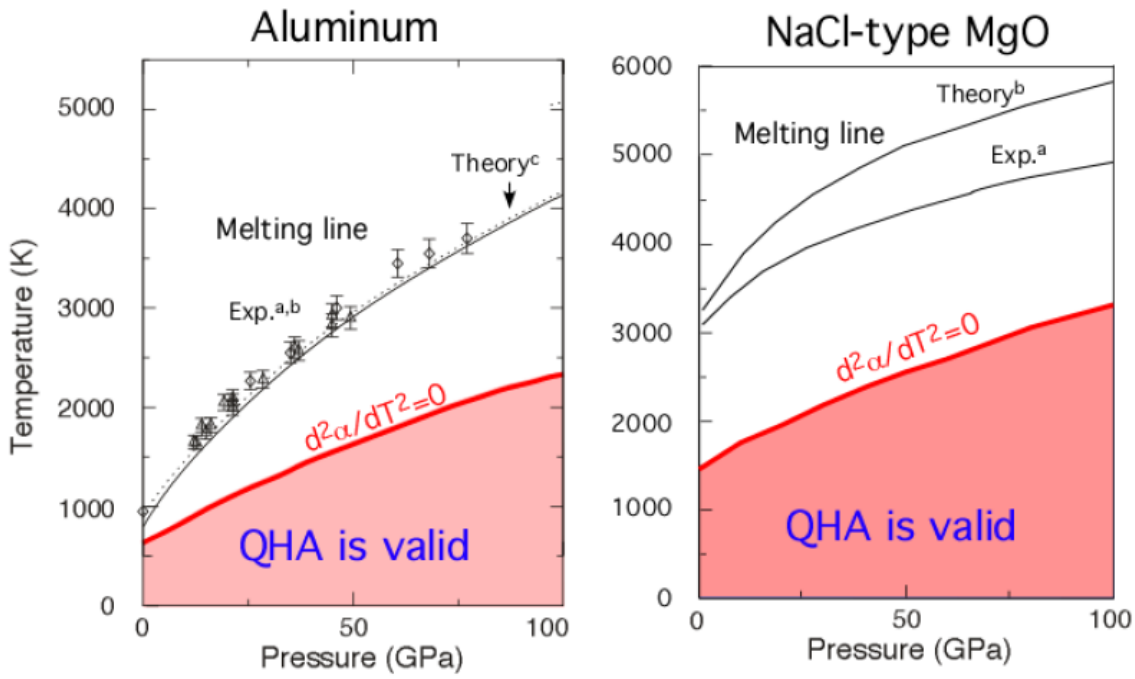
Aluminum
Temperature (K)
5000
4000
3000
2000
1000
0
Melting line
Theory^c
Exp.^a,b
d²α/dT²=0
QHA is valid
0
50
100
Pressure (GPa)
NaCl-type MgO
6000
5000
4000
3000
2000
1000
0
Melting line
Theory^b
Exp.^a
d²α/dT²=0
QHA is valid
0
50
100
Pressure (GPa)

Figure 10 -

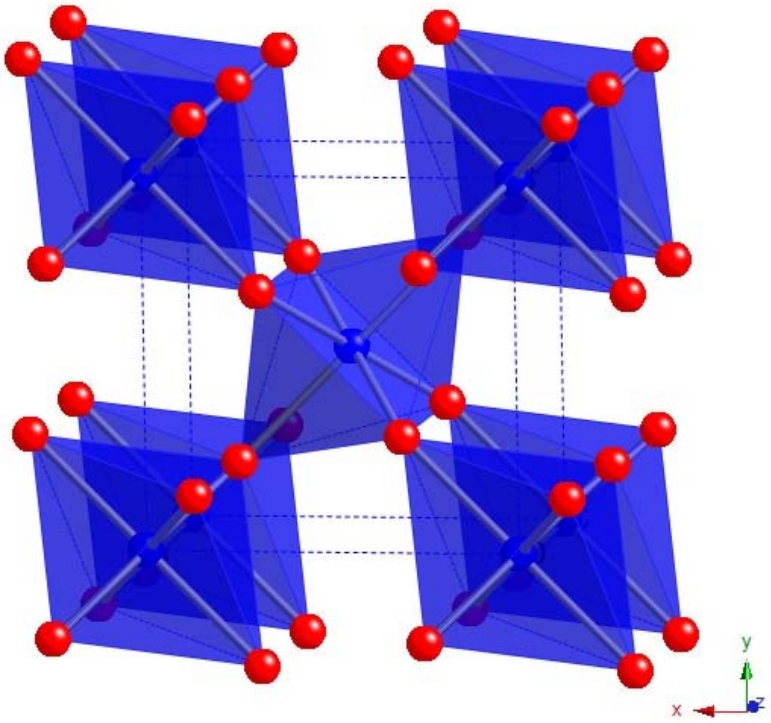

Figure 11 -

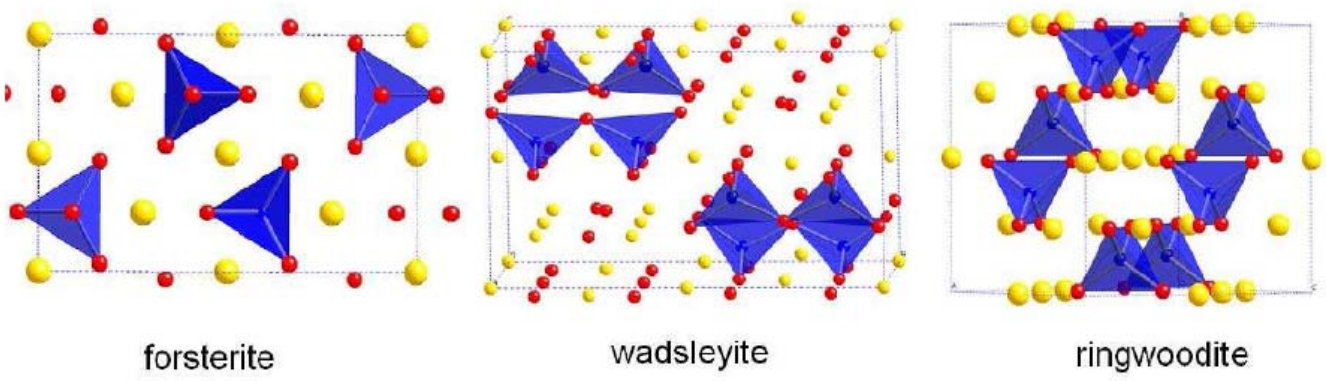

Figure 12 -

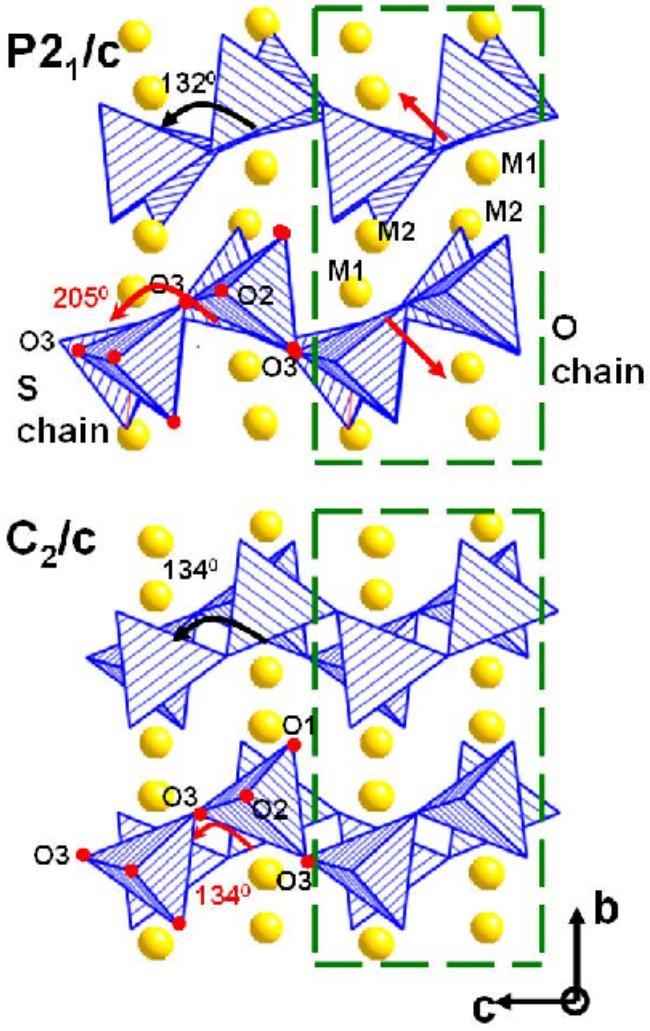
P2₁/c
132⁰
M1
M2
M2
M1
205⁰
O3
O2
O3
O3
S
chain
O
chain
C₂/c
134⁰
O1
O3
O2
O3
O3
134⁰
b
c

Figure 13 -

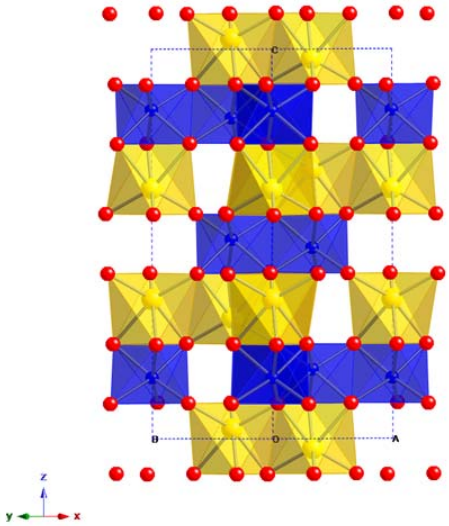

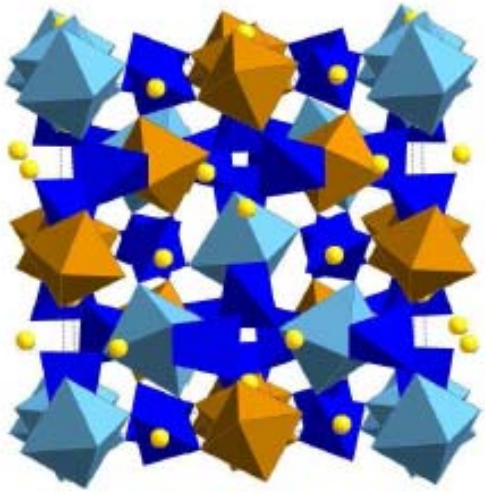

Figure 14 -

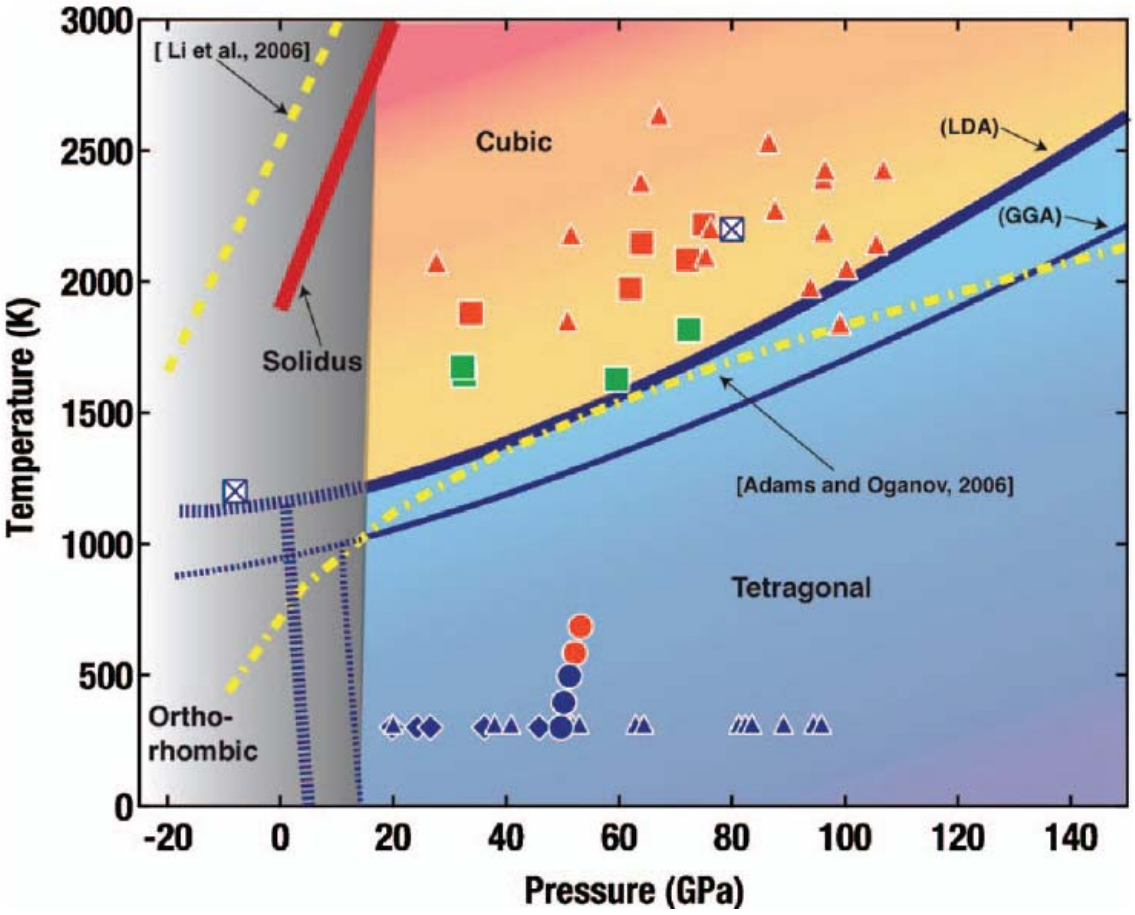
[Li et al., 2006]
Cubic
(LDA)
(GGA)
Solidus
[Adams and Oganov, 2006]
Tetragonal
Ortho-
rhombic
Temperature (K)
Pressure (GPa)
3000
2500
2000
1500
1000
500
0
-20
0
20
40
60
80
100
120
140

Figure 15

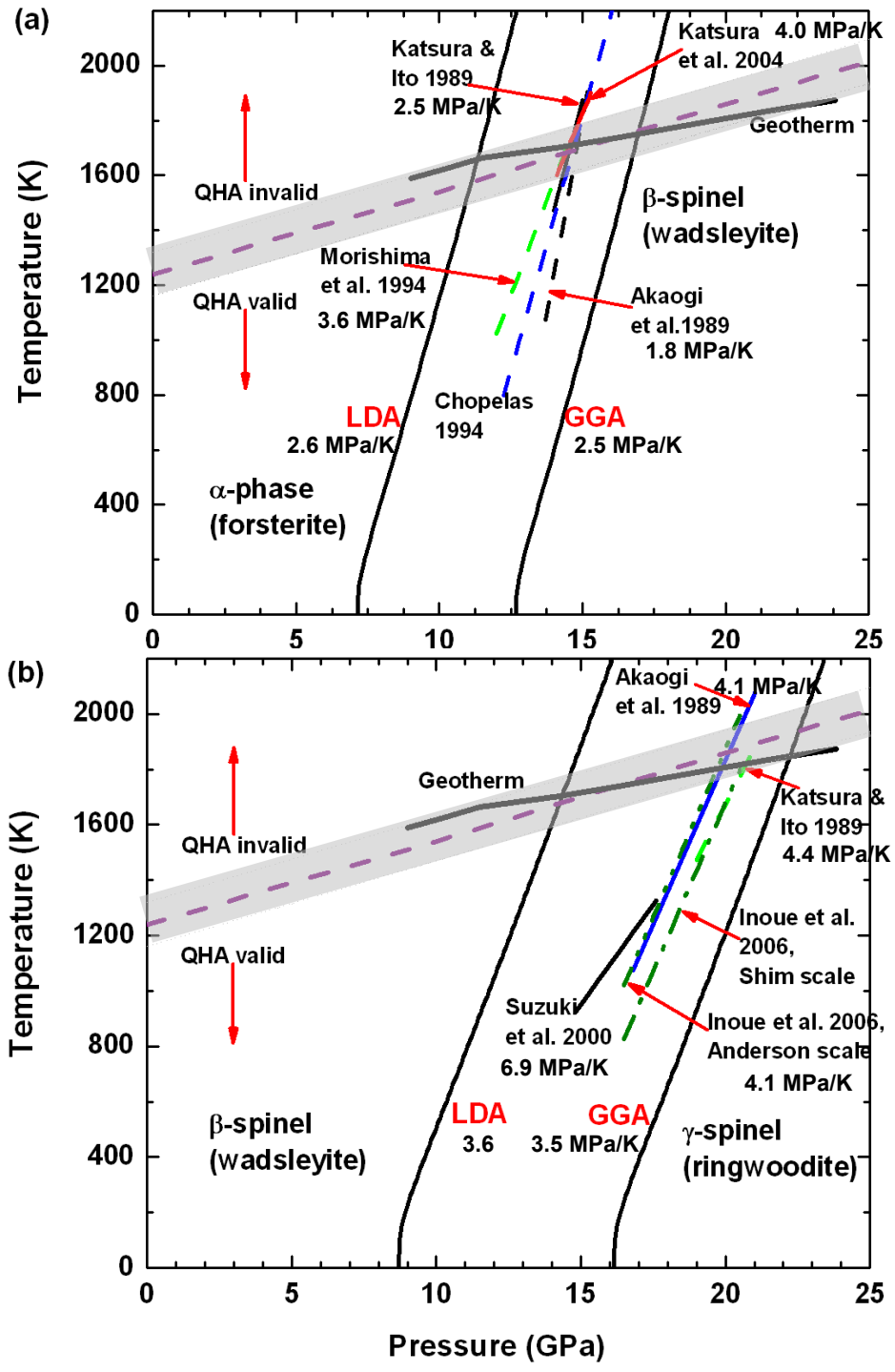
(a)
Temperature (K)
2000
1600
1200
800
400
0
0
5
10
15
20
25
Katsura &
Ito 1989
2.5 MPa/K
Katsura 4.0 MPa/K
et al. 2004
Geotherm
QHA invalid
β-spinel
(wadsleyite)
Morishima
et al. 1994
3.6 MPa/K
QHA valid
Akaogi
et al.1989
1.8 MPa/K
LDA
2.6 MPa/K
Chopelas
1994
GGA
2.5 MPa/K
α-phase
(forsterite)
(b)
Temperature (K)
Akaogi
et al. 1989
4.1 MPa/K
Geotherm
Katsura &
Ito 1989
4.4 MPa/K
QHA invalid
QHA valid
Inoue et al.
2006,
Shim scale
Suzuki
et al. 2000
6.9 MPa/K
Inoue et al. 2006,
Anderson scale
4.1 MPa/K
β-spinel
(wadsleyite)
LDA
3.6
GGA
3.5 MPa/K
γ-spinel
(ringwoodite)
Pressure (GPa)

Figure 16 -

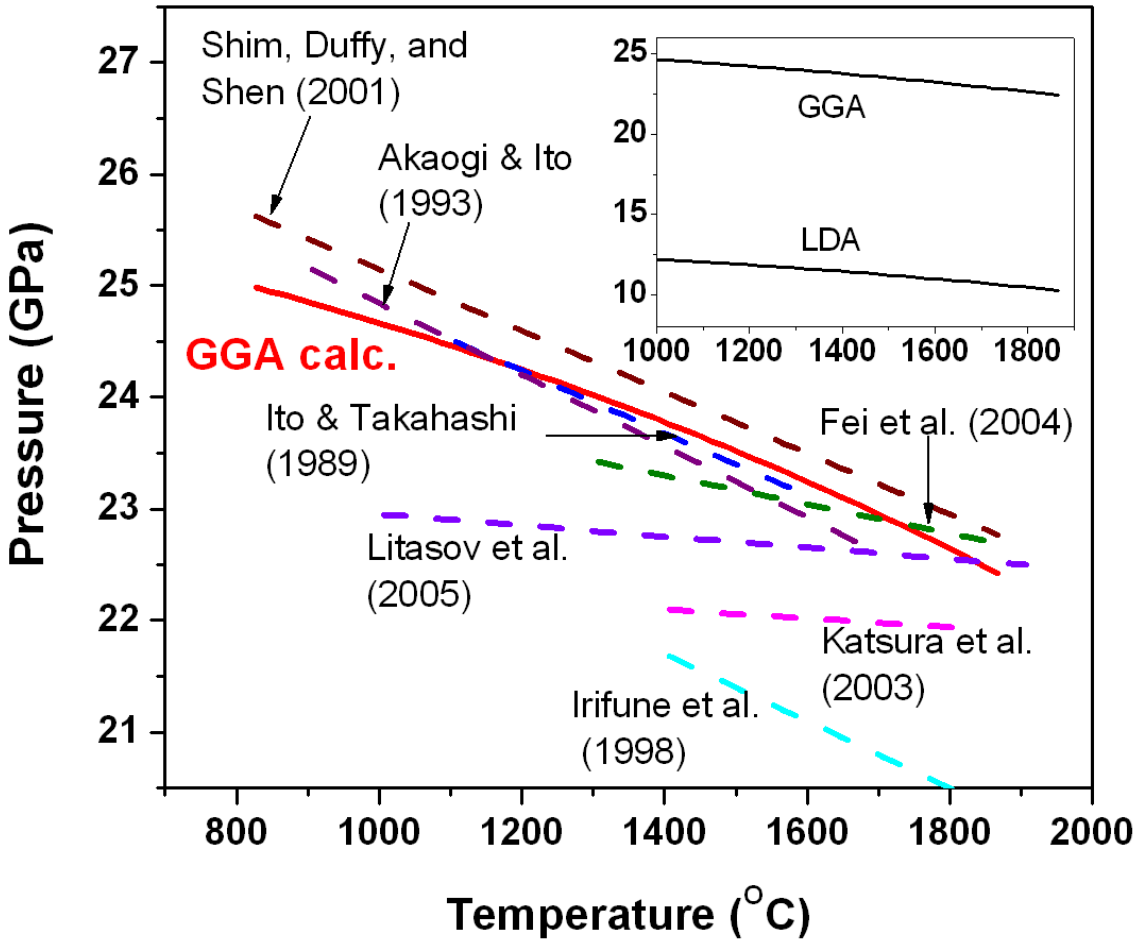
Shim, Duffy, and
Shen (2001)
Akaogi & Ito
(1993)
GGA calc.
Ito & Takahashi
(1989)
Litasov et al.
(2005)
Irifune et al.
(1998)
Katsura et al.
(2003)
Fei et al. (2004)
GGA
LDA
Pressure (GPa)
Temperature (°C)
27
26
25
24
23
22
21
800
1000
1200
1400
1600
1800
2000
25
20
15
10
1000
1200
1400
1600
1800

Figure 17 -

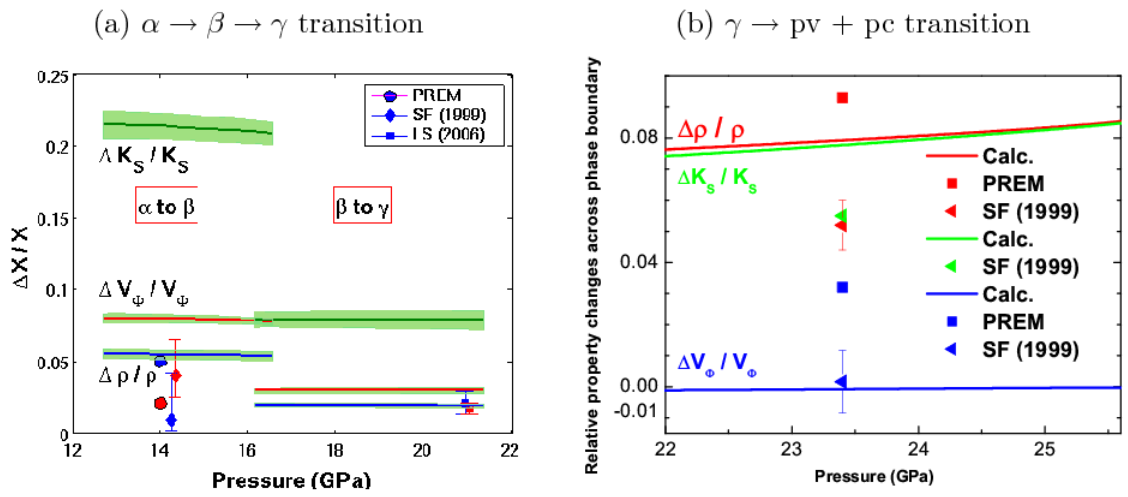
(a) $\alpha \rightarrow \beta \rightarrow \gamma$ transition
(b) $\gamma \rightarrow$ pv + pc transition
PREM
SF (1999)
IS (2006)
$\Delta K_S / K_S$
$\Delta V_\Phi / V_\Phi$
$\Delta \rho / \rho$
α to β
β to γ
ΔX / X
Pressure (GPa)
Relative property changes across phase boundary
Calc.
PREM
SF (1999)
Calc.
SF (1999)
Calc.
PREM
SF (1999)

Figure 18 -

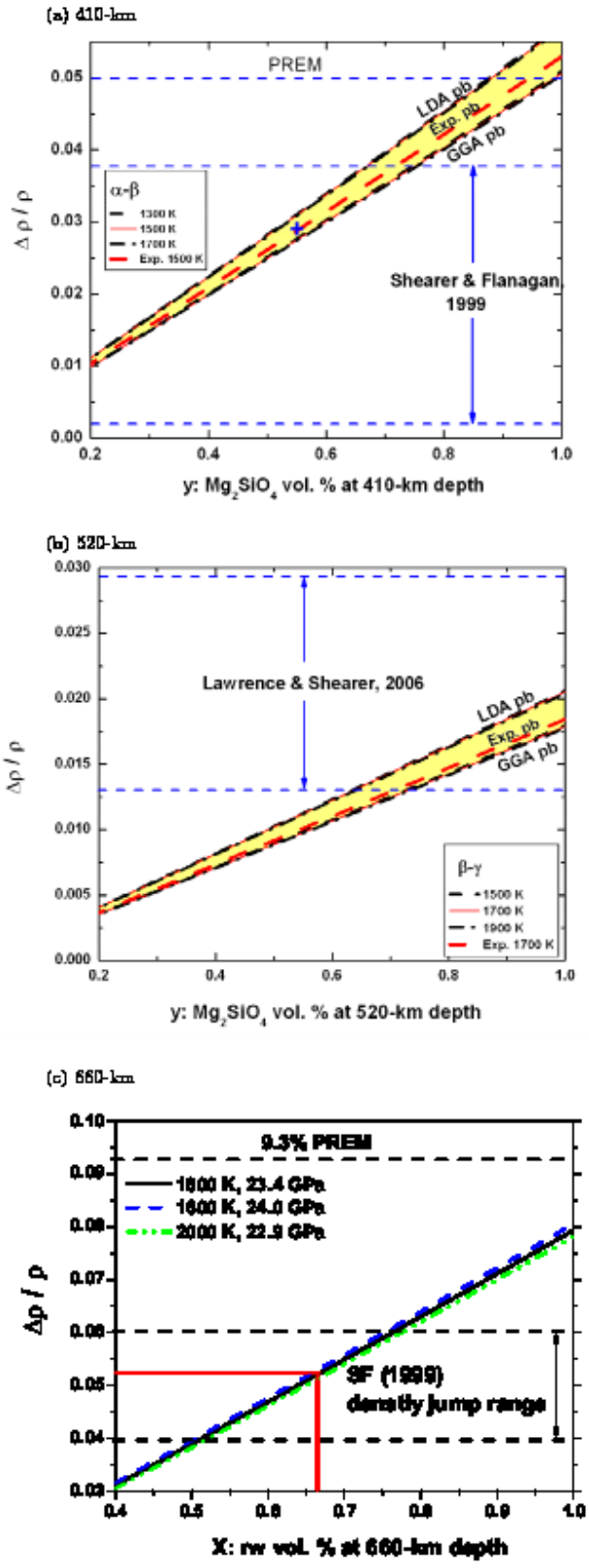
(a) 410-km
PREM
LDA pb
Exp. pb
GGA pb
α-β
1300 K
1500 K
1700 K
Exp. 1500 K
Shearer & Flanagan, 1999
Δ ρ / ρ
y: Mg2SiO4 vol. % at 410-km depth
(b) 520-km
Lawrence & Shearer, 2006
LDA pb
Exp. pb
GGA pb
β-γ
1500 K
1700 K
1900 K
Exp. 1700 K
Δρ / ρ
y: Mg2SiO4 vol. % at 520-km depth
(c) 660-km
9.3% PREM
1600 K, 23.4 GPa
1600 K, 24.0 GPa
2000 K, 22.9 GPa
SF (1999) density jump range
Δρ / ρ
X: rw vol. % at 660-km depth

Figure 19 –

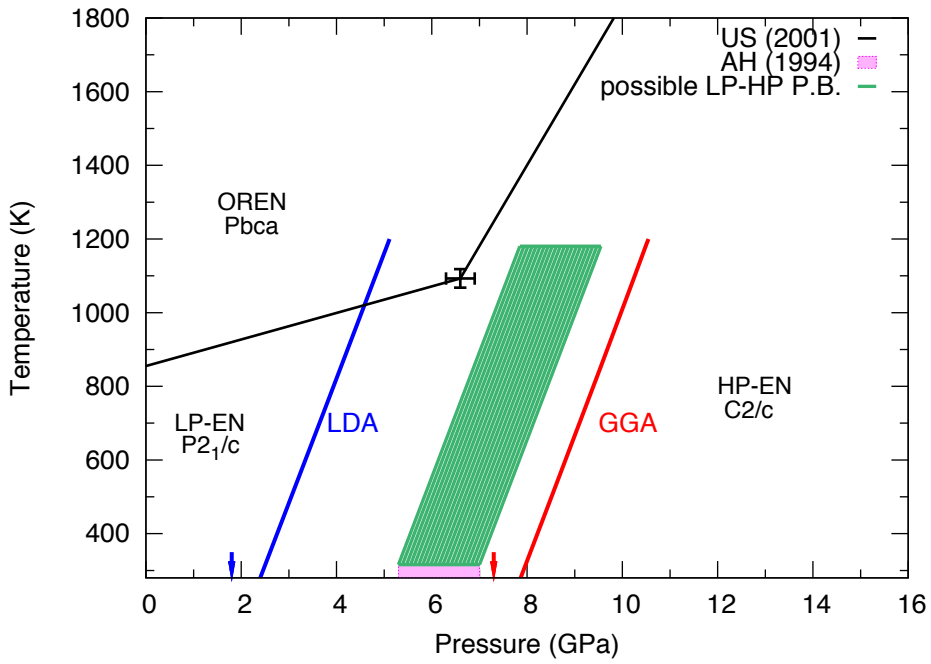
US (2001)
AH (1994)
possible LP-HP P.B.
OREN
Pbca
LP-EN
P2$_1$/c
LDA
GGA
HP-EN
C2/c
Temperature (K)
Pressure (GPa)
1800
1600
1400
1200
1000
800
600
400
0
2
4
6
8
10
12
14
16

Figure 20 -

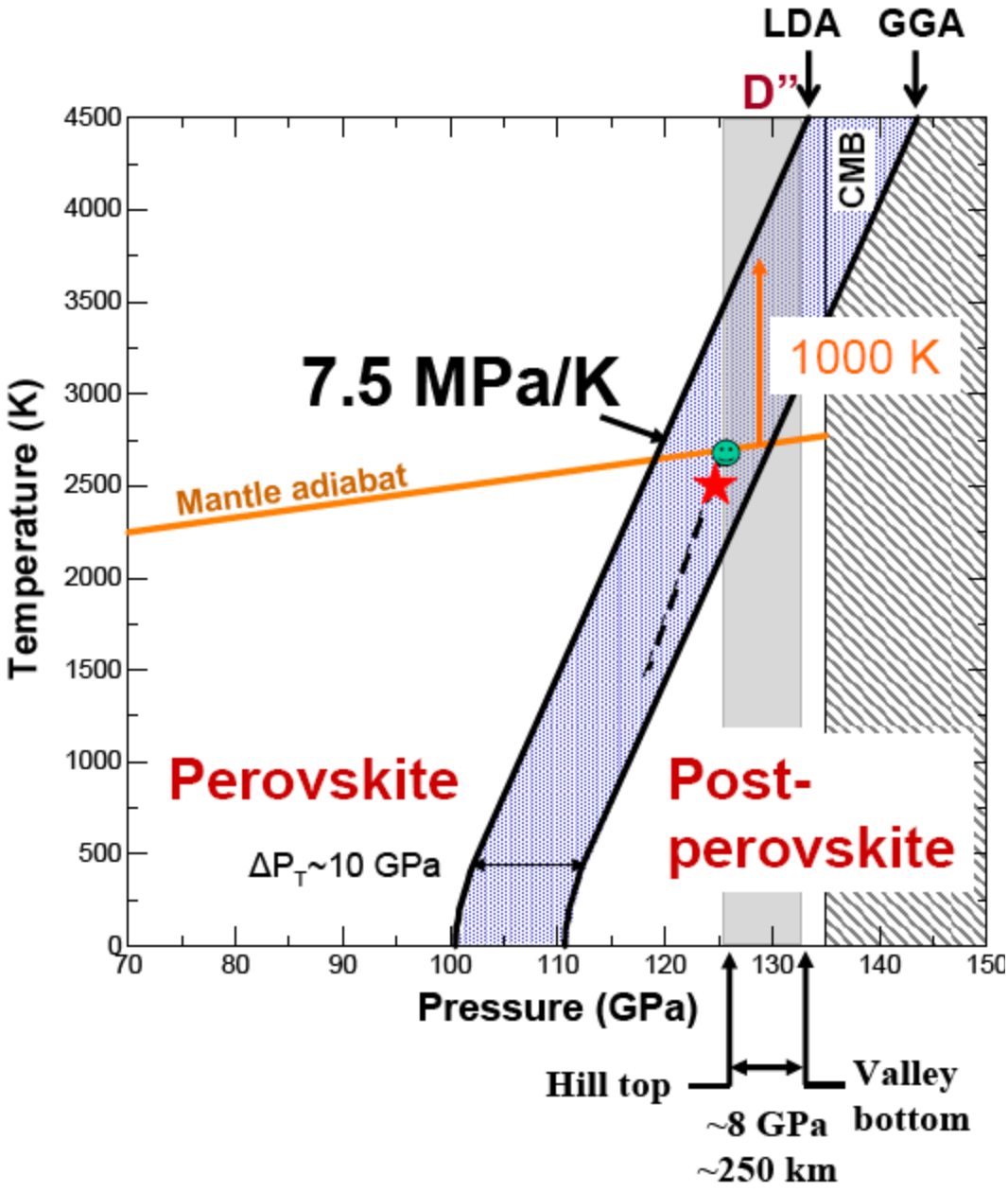
LDA
GGA
D''
CMB
1000 K
7.5 MPa/K
Mantle adiabat
Perovskite
Post-perovskite
ΔP_T~10 GPa
Temperature (K)
Pressure (GPa)
Hill top
Valley bottom
~8 GPa
~250 km

Figure 21 -

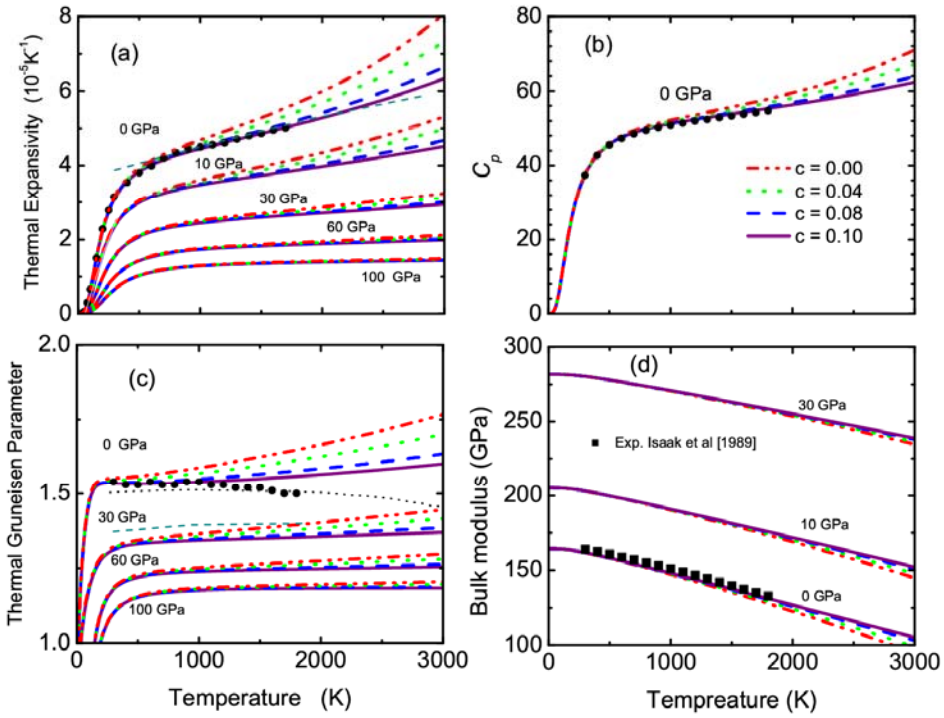
(a)
Thermal Expansivity (10^{-5}K^{-1})
0 GPa
10 GPa
30 GPa
60 GPa
100 GPa
(b)
C_p
0 GPa
c = 0.00
c = 0.04
c = 0.08
c = 0.10
(c)
Thermal Gruneisen Parameter
0 GPa
30 GPa
60 GPa
100 GPa
Temperature (K)
(d)
Bulk modulus (GPa)
30 GPa
Exp. Isaak et al [1989]
10 GPa
0 GPa
Tempreature (K)

Figure 22 -

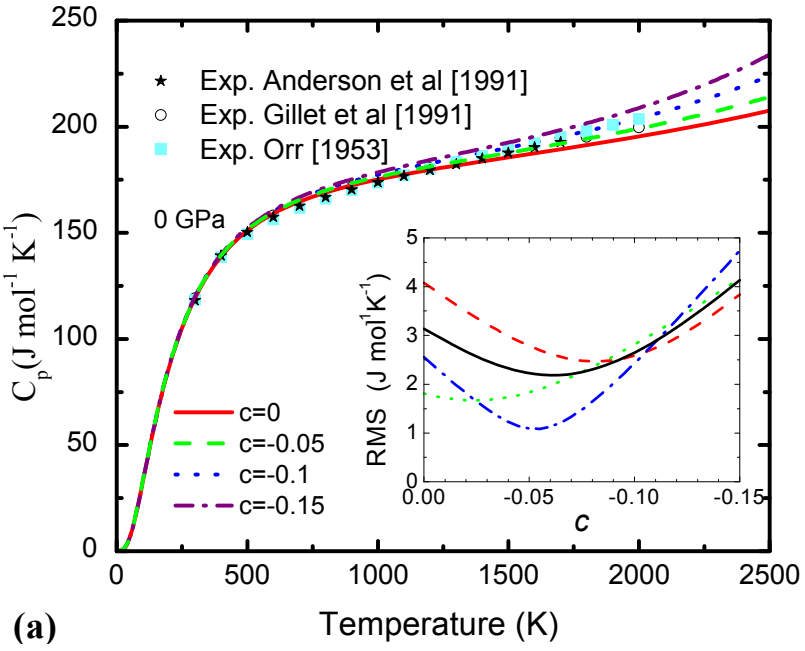
Exp. Anderson et al [1991]
Exp. Gillet et al [1991]
Exp. Orr [1953]
0 GPa
c=0
c=-0.05
c=-0.1
c=-0.15
RMS (J mol^{-1}K^{-1})
c
C_p(J mol^{-1} K^{-1})
Temperature (K)

(a)

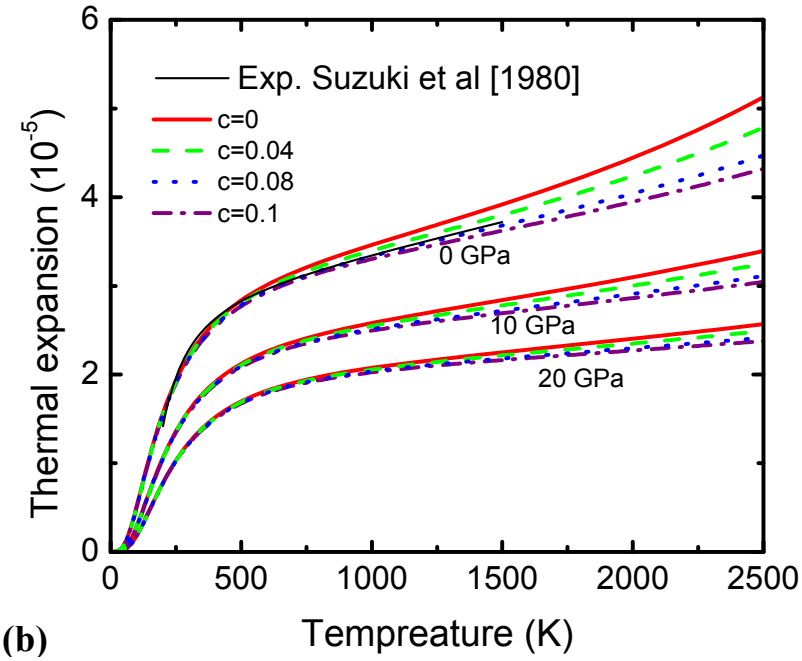
Exp. Suzuki et al [1980]
c=0
c=0.04
c=0.08
c=0.1
0 GPa
10 GPa
20 GPa
Thermal expansion (10^{-5})
Tempreature (K)

(b)

Figure 23 --

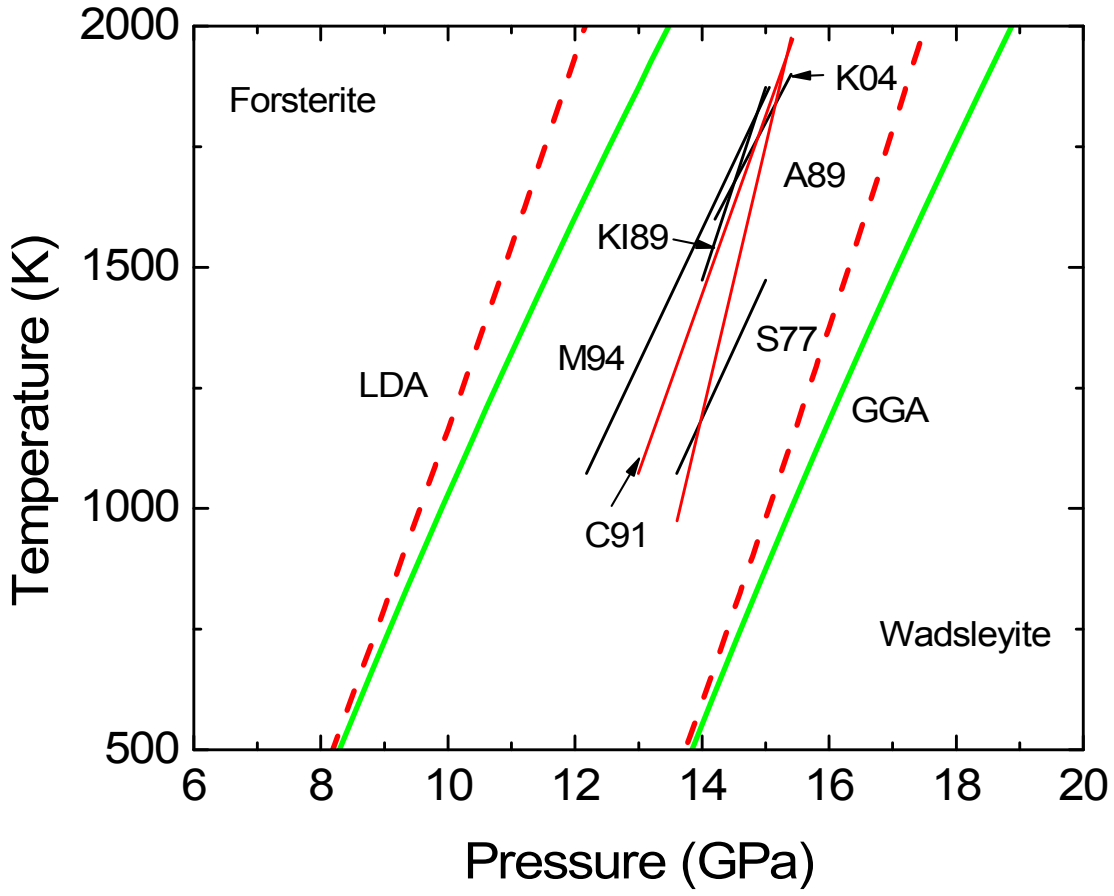
2000
1500
1000
500
Temperature (K)
6
8
10
12
14
16
18
20
Pressure (GPa)
Forsterite
Wadsleyite
LDA
GGA
K04
A89
KI89
M94
S77
C91

Figure 25 -